Geomechanics and Engineering, *Vol. 42, No. 5 (2025) 347-372*
https://doi.org/10.12989/gae.2025.42.5.347

An examination of stress wave blasts deflection in materials that resemble rocks with soft and hard interlayers

Mojtaba Pourali[1], Vahab Sarfarazi*[1], Hesam Dehghani[1], Hadi Haeri[2], Jinwei Fu[3], Shirin Jahanmiri[1] and Mohammad Fatehi Marji[4]

[1]*Department of Mining Engineering, Hamedan University of Technology, Hamedan, Iran*
[2]*Department of Mining Engineering, Higher Education Complex of Zarand, Shahid Bahonar University of Kerman, Kerman, Iran*
[3]*School of Civil Engineering and Transportation, North China University of Water Resources and Electric Power, Zhengzhou, 450046, China*
[4]*Department of Mine Exploitation Engineering, Faculty of Mining and Metallurgy, Institute of Engineering, Yazd University, Yazd, Iran*

(*Received May 13, 2025, Revised August 22, 2025, Accepted August 26, 2025*)

Abstract. This study employs the particle flow algorithm to simulate stress wave propagation across stuffed joints in a single-hole blasting scenario involving concrete with soft and stiff interlayers. Blasting was conducted at different depths, locations, and interlayer thicknesses, followed by analysis of the energy field and crack development. Results showed that shear fractures formed perpendicular to tensile cracks, which developed parallel to the blast hole. Increasing the hard interlayer's thickness enhanced its capability to accommodate concrete failure and reflect stress waves. The proximity of the weak interlayer to the blast hole influenced damage in the surrounding rock, with a threshold radius roughly twice the blast area. Outside this radius, the effects of blasting were minimal. For fixed weak interlayers, greater thickness led to more stress wave reflection and worsened concrete collapse. Lengthening weak interlayers improved stress reduction, while shortening them decreased the peaks of angular momentum and friction potential, increasing strain energy. In contrast, lengthening hard interlayers reduced effective stress dispersion and lowered both kinetic and friction energy peaks. The stress states of an object show that when a weak interlayer is within a radius of approximately twice the crushing area, the surrounding host concrete experiences high stress. In contrast, stress is low when the weak interlayer is outside this radius. When a hard interlayer is included, the host concrete is under high stress regardless of distance. The soft interlayer model exhibits higher kinetic and overall friction energy peaks compared to the hard interlayer model, but has a lower strain energy peak due to its significant dampening effect on wave propagation.

Keywords: blasting; hard interlayer; PFC2D; physical test; soft interlayer

1. Introduction

To economically break apart rocks, techniques such as drilling and blasting are commonly employed in various applications, including mining, underground power plants, tunnels, and excavation projects. When an explosive is detonated, a large amount of energy is rapidly released, impacting the walls of the borehole and resulting in rock damage, fractures, and fragmentation, including secondary fragmentation. This process is essential for achieving effective rock fragmentation. Rock masses typically contain multiple joint sets that influence their mechanical behavior. Weak structural features such as joints, faults, and interlayers can cause refraction, reflection, and waveform conversion, which in turn reduce the effectiveness of the blasting energy. By carefully selecting the blasting position and considering the construction and structural qualities of the rock mass, we can save significant amounts of dynamite, enhance blasting efficiency, protect the rock during excavation, and increase the stability of the rock mass. Predicting wave absorption in jointed rock masses is vital for protecting subsurface geotechnical infrastructure from seismic and blasting stress waves. Most studies have focused on the seismic responses of joints. The attenuation of stress waves that travel through empty joints has been extensively investigated, taking various deformation behaviors into account through the use of displacement discontinuity models (Zhao and Cai 2001, Zhao *et al.* 2006, Wright 2010, Bidgoli and Jing 2014, Woo *et al.* 2015, Haeri 2015a, b, c, d, Shuraim *et al*. 2016, Shaowei *et al*. 2016, Akbas 2016, Yaylacı 2016, Sarfarazi and Haeri 2017, Li *et al*. 2018, Xue *et al.* 2019, Liu 2020, Bai *et al*. 2020, Qian *et al.* 2020, Naeimi *et al*. 2021, Öner *et al.* 2022, Fuyad *et al*. 2024, Golewski 2024a, b, c, d, Sekban *et al*. 2025). Zhou and He (2013) compared the failure modes of jointed rocks and complete rocks, showing that the geometric distribution, alongside the mechanical and structural qualities of the joints, significantly influences the blasting damage model. Liu (2011) established a damage constitutive relationship for irregular joints, developing an analytical approach to investigate the behavior of stress waves, including both reflection and transmission. This

*Corresponding author, Ph.D.
E-mail: vahab.sarfarazi@gmail.com

ISSN: 2005-307X (Print), 2092-6219 (Online)

research revealed important theoretical insights into the relationships between reflections, transmissions, and fractal dimensions. In 2008, Abdellah conducted an analysis involving 16 groups of model experiments with varying incidence angles and detonation positions to study fragmentation distribution. The results indicated that both the location of the explosive and the orientation of the joints considerably affect the blasting outcomes. Interestingly, unfilled joints present a unique situation in nature. These joints are often filled with materials such as sand, clay, worn rock, and/or hard rock, which can be several centimeters thick. The mechanical behavior of the granite mass is notably influenced by the type of fill material used (Barton 1974, Wang *et al.* 2020). It is essential to examine the seismic response of filled joints. Modifications to the Split Hopkinson Pressure Bar (SHPB) have facilitated several experimental studies aimed at understanding the vibration characteristics of these joints. In their research on the dynamic formability of filled joints, Li *et al*. (2009, 2013, 2014) considered various fill thicknesses and water contents. Their research revealed a nonlinear connection between pressure and the sealing of filled joints when subjected to normal dynamic loads. Additionally, Wu *et al.* (2012a, b, 2013a, b, 2014) conducted experimental studies on the transient behavior of joints filled with quartz sand. Simultaneous displacement and stress are disrupted when the stress wave hits the filled joints. Additionally, the seismic response of the filled joint is greatly affected by the loading rate. Additionally, some analytical models have been presented that treat the filled joint as an independent element. In seismological theory, the filled joint is often represented simply as a constant elastic or viscoelastic thin layer, with a thickness equal to L, positioned between the surrounding rocks (Fig. 1, Brekhovskikh 1960, Zhu *et al*. 2012, Yang *et al.* 2019, Shu *et al*. 2025). The connections formed by a thin coating of media are often regarded as fixed, implying that when a stress wave impacts the interfaces, both the displacement and stress remain continuous. However, in these thinner layers, when stress waves propagate across a filled joint, the stress and displacement between the front and rear junctions can be discontinuous due to the significant influence of the accumulated material.

Zhu *et al*. (2011) proposed a model that accounts for displacement and stress discontinuities to investigate the vibration characteristics of joints using viscoelastic materials. Unfortunately, this thin layer model can be inaccurate when considering the geological features of the specified joint. When loaded, the fill material not only undergoes elastic deformation but also experiences plastic deformation. Consequently, it is anticipated that an elastic-plastic model will provide a better representation of the overall deformation mechanism of a filled joint.

Typically, the filled layer lacks tensile strength. As a result, when a compressive force is applied to the filled joint, the stress associated with dislocation between the front and rear contacts becomes discontinuous due to the gap between the various foreground rocks and the fill material. Furthermore, the loading and unloading characteristics of the filled joint must be considered. Researchers have found that only when these

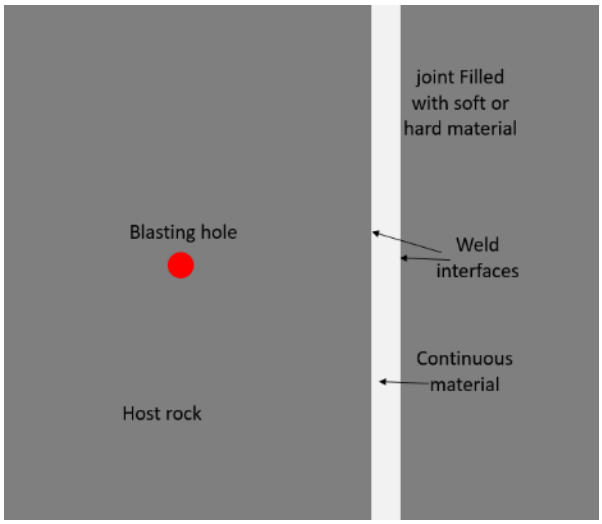

Fig. 1 Thin layer medium model

loading/unloading effects are taken into account do the analytical results align closely with experimental outcomes (Ma *et al*. 2011, Fan and Wong 2013).

Establishing an analytical model that fully takes into account all of the aforementioned factors is frequently challenging. Numerical analysis is often a practical and affordable solution to examine the seismic performance of filled joints. The calculation of acoustic waves in structural behavior and also in filled granular materials is the major topics of a few more study of numerical simulation that have been conducted in this area. In earlier research, wave propagation in the granular media was frequently simulated using particle models based on the discrete element method (DEM) (Thomas *et al*. 2009, Zamani and El Shamy 2011, Marketos and O'Sullivan 2013). Few researchers are able to perform in-depth assessments either from viewpoint of each individual failure characteristic of rock mass utilizing hard interlayer for such difficulty of weak interlayer across natural rock mass since most researchers approach it from the broad perspective of theoretical formulation or engineering. Therefore, in this paper, blasting frameworks of rock mass with both an external and internal interlayer are established in order to increase the controllability of the blasting effect but instead complement this same investigation mostly on blasting of rock mass of interlayers. These models are based on laboratory assessment and discrete element software. The blasting characteristics are then examined using the fractured impact, stress domain, and energy field views.

By increasing the length of the interlayer in weak interlayers, stress reduction was enhanced. Conversely, decreasing the interlayer length resulted in lower peaks for both kinetic energy and frictional energy. Shortening the interlayer length also led to an increase in strain energy.

In the case of hard interlayers, lengthening the interlayer significantly decreased stress attenuation. Additionally, extending the interlayer resulted in lower peaks for both kinetic and friction energy. Consequently, increasing the interlayer length also raised the strain energy.

The soft interlayer model exhibited a higher peak in kinetic energy and overall friction energy compared to the

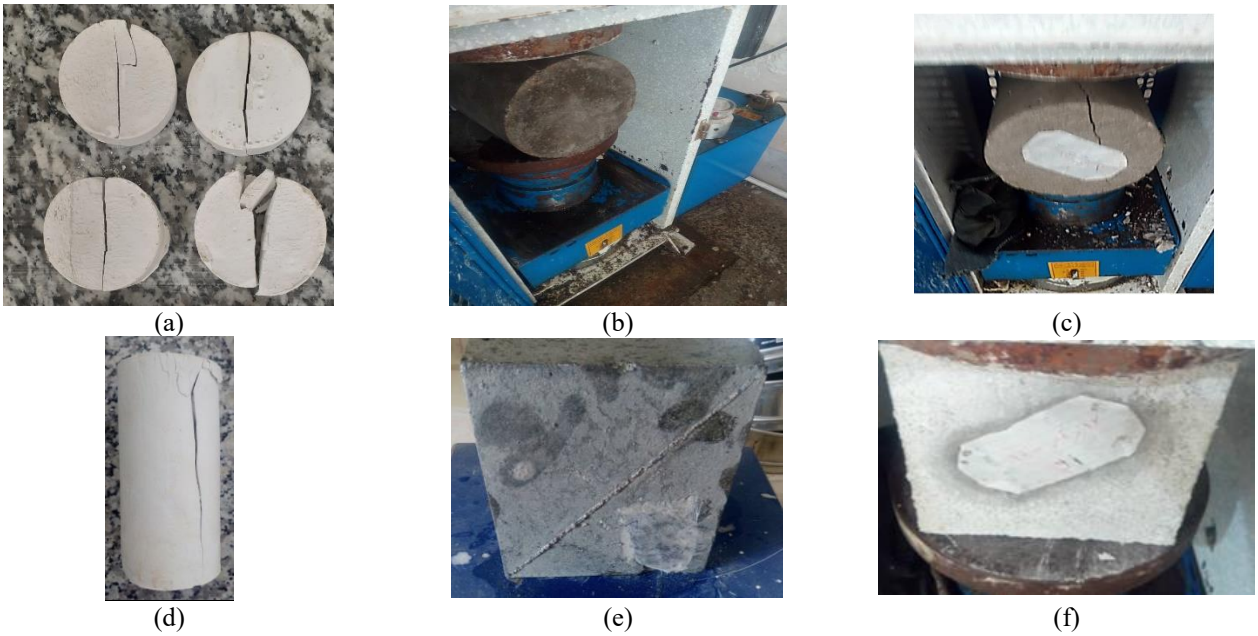

Fig. 2 Failure patterns were observed in the following structures: (a) gypsum disc, (b) strengthening of concrete disc, (c) low shear strength concrete disc, (d) gypsum cylinder and (e) strengthening of concrete rectangle and poor stability concrete rectangle

Table 1 Mechanical properties of either the components

Hard concrete's tensile strength	3.1MPa
Gypsum's ability to sustain tension	0.7 MPa
Brittle concrete's tensile strength	1.45MPa
Concrete with a high compressive strength	43 MPa
Compressive strength of gypsum	8.6 MPa
Compressive strength of soft concrete	22 MPa

hard interlayer model. However, the soft interlayer model had a lower strain energy peak than the hard model. This difference is primarily due to the substantial effect of the host concrete's soft interlayer on dampening wave propagation.

2. Experimental test

2.1 Concrete and gypsum sample' mechanical behavior

This research centered on a soft concrete sample as the foundational material. Two distinct interlayers were created: soft gypsum and hard concrete. The gypsum used in this study was mixed at a ratio of 1.4 parts gypsum to 1 part water. The specimens for high-strength and low-strength concrete were produced using a combination of cementitious materials, silica fume, water, a superplasticizer, and both fine and coarse aggregates. The mix designs for the concrete samples varied between the high-strength and low-strength specimens.

The high-strength concrete mixture included 6.8 kg/m³ of a highly plasticizing agent, 25 kg/m³ of silica fume, 168 kg/m³ of water, 810 kg/m³ of precise infill, 810 kg/m³ of granular aggregate, and 500 kg/m³ of Portland cement. In contrast, the low-strength concrete mixture comprised 6.8 kg/m³ of the same highly plasticizing agent, 15 kg/m³ of silica fume, 190 kg/m³ of water, 40 kg/m³ of precise infill, 510 kg/m³ of granular aggregate, and 300 kg/m³ of cement. These compositional differences highlight the variations in strength and performance characteristics between the two types of concrete.

For testing, cylindrical and disc specimens were subjected to uniaxial compressive tests and Brazilian tensile tests. The disc specimens had a diameter of approximately 54 millimeters and a thickness of 27 millimeters, while the cylindrical specimens measured 54 millimeters in diameter and 108 millimeters in height.

Figs. 2(a)-2(c) illustrate various failure modes observed during the Brazilian tensile tests for the gypsum, low-strength concrete, and high-strength concrete samples. Figs. 2(d)-2(f) depict the causes of failure in the uniaxial tests for the same materials.

Table 1 illustrates the tensile strength but instead compressive strength for something like the samples of high strength concrete, gypsum, and low strength concrete. It should be noted that low strength concrete has more strength than gypsum. To verify the accuracy of the measurements, all tests reported in this paper were performed three times, and the average findings are presented here.

2.2 How to make concrete block containing internal hole and both of the soft and hard interlayers

As shown in Fig. 3(a), the main frame is cubic with dimension of 700 mm × 700 mm × 300 mm. A specific plastic fiber with 700 m × 700 m × 10 mm was placed into

(a) (b) (c) (d)

Fig. 3 (a) Frame (b) The oily frame was filled with a particular plastic fiber, which was marked with the specifications for a wood slab and a plastic cylinder. (c) The mold was filled with concrete. (d) the wooden slab and plastic cylinder were both removed after the concrete had dried (f) Hard concrete and gypsum were put into the notch

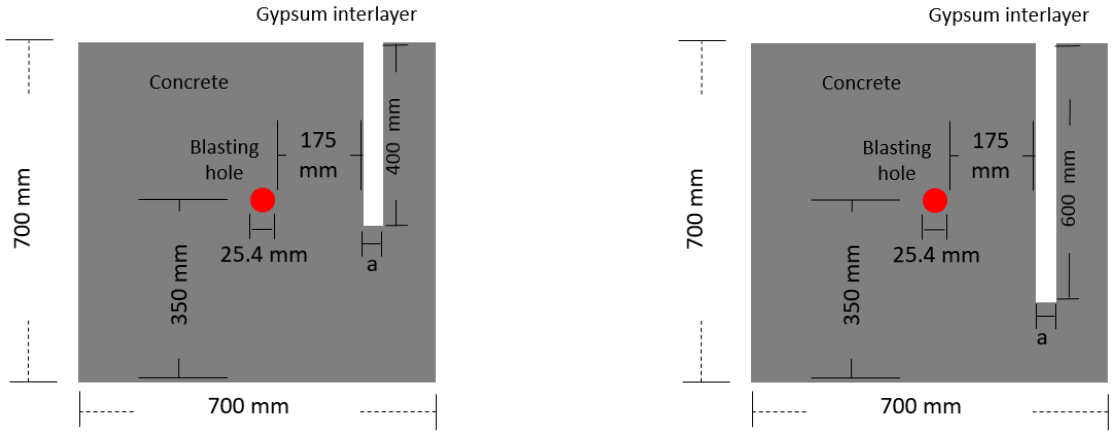

(a) (b)

Fig. 4 Schematic view of sample geometry, (a) gypsum interlayer with length of 400 mm and (b) gypsum interlayer with length of 600 mm

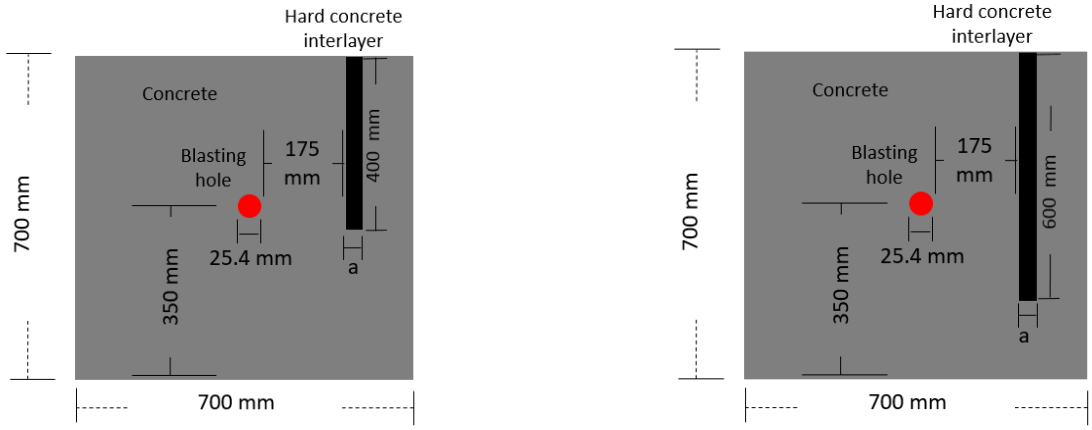

(a) (b)

Fig. 5 Schematic view of sample geometry, (a) hard concrete interlayer with length of 400 mm and (b) hard concrete interlayer with length of 600 mm

the oily frame (Fig. 3(a)). One plastic cylinder and one wood slab were specified on the plastic fiber (Fig. 3(a)). In the first stage, the concrete was poured into the mold (Fig. 3(b)). Both of the plastic cylinder and wood slab were removed when the concrete was hardened (Fig. 3(c)). One hole and one edge notch were created in the concrete block. The samples were merged in water for 21 hours. Then, both of the gypsum interlayer and hard concrete interlayer were poured into the notch (Fig. 3(d)). Fig. 4 shows the schematic view of sample geometry. Interlayers have three

(a) (b) (c) (d)

Fig. 6 Blasting pattern

Fig. 7 Failure pattern

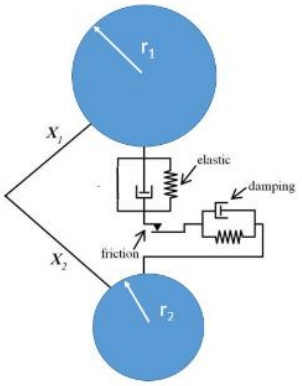

Fig. 8 Contact bond between particles

different wide (a in Fig. 4); i.e., 150 mm, 300 mm and 450 mm (Fig. 4). Diameter of hole was 25.4 mm. Distance between the central hole and interlayers was 175 mm. Interlayers lengths were 400 mm and 600 mm (Figs. 4 and 5).

2.3 In-situ test procedure

For blasting action, 100 gr emolliate was used per hole with electric detonators as shown in Fig. 6. Fig. 7 shows the failure pattern of concrete samples. Studying how interlayers affect fracture qualities is impossible due to the blasting energy's extreme strength.

3. Particle flow code

PFC is based on a classical numerical technique known as the discrete element method. It specifically utilizes the flat joint (FJ) model within this framework to accurately simulate brittle materials, such as rocks, particularly those with high compressive-to-tensile strength ratios. The interface is divided into elements, and forces are updated based on the behavior of the bonds during interactions between grains.

Two fundamental components of the simulation analysis inside the particle flow code are the particle and the contact. Particle contact can transmit load, replicating the mechanical characteristics of rock (Fig. 8).

If the concentrated strength limit is reached, the connection must fail, the same two particles must separate from one another, and the program will detect that there is a fracture observed between the two particles. This same flat joint model (FJM) is utilized in this study, and the model's failure criteria are displayed in formula (1). When the shear stress (τc) reaches the maximum shear strength ($\tau c > \tau max$) or the tensile stress (σc) surpasses the maximum tensile strength ($\sigma c > \sigma tmax$), the bonded interface ruptures,

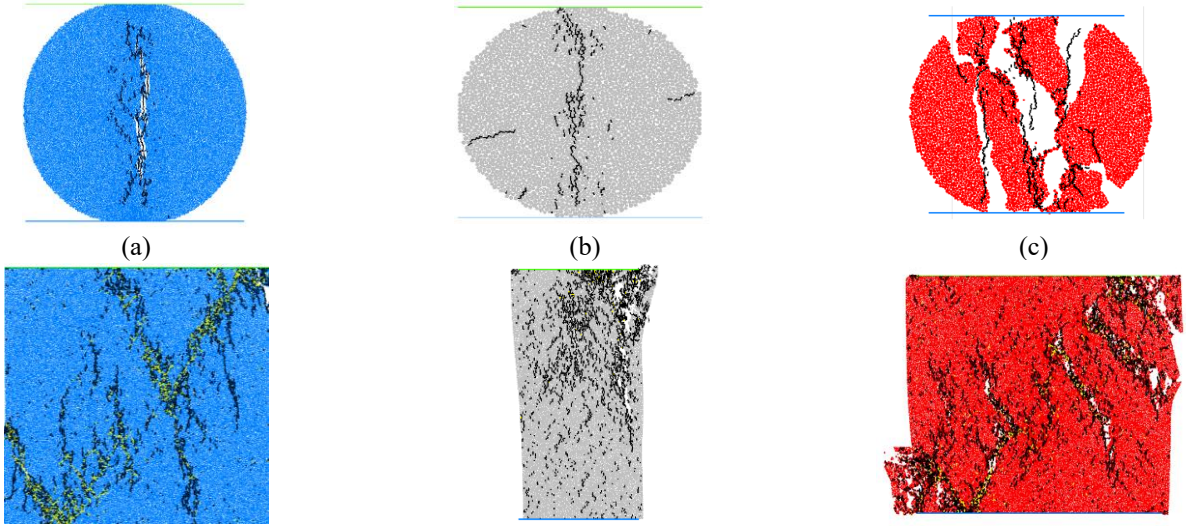

Fig. 9 (a) Brazilian experiment using poor concrete, (b) test on gypsum conducted in Brazil, (c) Brazilian test on concrete with great strength, (d) Low strength concrete underwent a uniaxial test, (e) Uniaxial test on gypsum and (f) Uniaxial test on high strength concrete

Table 2 Mechanical properties of numerical model

Concrete with a high-tensile strength (MPa)	3.15	compression strength of high strength concrete (MPa)	43.3
Gypsum's tensile strength (MPa)	0.7	Gypsum's compression strength (MPa)	8.9
Concrete with lower strength tensile strength (MPa)	1.4	concrete with low strength's compressive strength (MPa)	21.5

creating a new fracture. The whole rock sample's particle and contact counts are known. The degree of the rock's damage increases as the number of consecutive cracks in a given range. As a result, within a limited range, the statistical variation in the frequency of fractures might also represent this same severity of rock collapse.

$$\sigma_{t\,max} = \frac{\overline{F_n}}{A} + \frac{|\bar{M}|}{I}\bar{R} \ , \qquad \tau_{max} = \frac{\overline{F_S}}{A} \tag{1}$$

where another ultimate normal stress and also optimum shear stress, respectively, are denoted by τmax and σtmax. The standard and tangential components of the force (F) are denoted by the letters Fn and FS, respectively. The bond cross section's area associated inertial moment are denoted as A and I, respectively. The bond radius is R. (Potyondy 2003).

3.1 Calculating and preparing the numerical models

Both the Uniaxial compaction as well as the Brazilian tensile strength examination, which are established tests for geo-mechanical applications, is employed to calibrate the numerical modeling approach (i.e., PFC2D) in this study.

The component assemblage of the geomaterial specimen that was modeled has to be standardized, according to several studies (Potyondy 2003, Ghazvinian 2012, Sarfarazi 2021). Gypsum, brittle concrete, and hard concrete are all simulated by using a flat joint model (FJM) within PFC2D. The Poisson's relationship was evaluated based on fluctuations in various ordinary and shear flexibility ratios, the Young modulus, and several other carefully selected micro-parameters. The bonding strengths of things like the components in the arrangement get calibrated by keeping the other characteristics (including friction angle, density, and plate diameters) constant throughout the calibration phase. The Micro-scale parameters of Young's modulus affect the elastic modulus of larger models. The relationship between normal stiffness and shear stiffness influences the Poisson's ratio in these models. Cohesion and tensile strength play a role in determining the uniaxial compressive strength and tensile strength of larger models, respectively. Furthermore, their standard deviations govern the stress level at which cracks begin to form.

The conventional microparameters for gypsum, high-strength concrete, and low-strength concrete include specific measurements and properties that are essential for modeling. The modeling height is 108 mm for gypsum and 150 mm for both high-strength and low-strength concrete, while the model width is 54 mm for gypsum and 150 mm for the concretes. All three materials share a smallest particle diameter of 0.9 mm and a finer particle diameter of 1.1 mm. In terms of density, gypsum has a density of 2400 kg/m³, high-strength concrete has 3000 kg/m³, and low-strength concrete has 2900 kg/m³. The elasticity modulus of contact is 2 GPa for gypsum, 4 GPa for high-strength concrete, and 3 GPa for low-strength concrete, with a common frequency of gaps set at 0.5. Friction angles measure 38° for gypsum, 40° for high-strength concrete, and 37° for low-strength concrete. Tensile strength values are 0.1 MPa for gypsum, 1.5 MPa for high-strength concrete, and 1 MPa for low-strength concrete, with corresponding standard deviations of 0.01 MPa, 0.15 MPa,

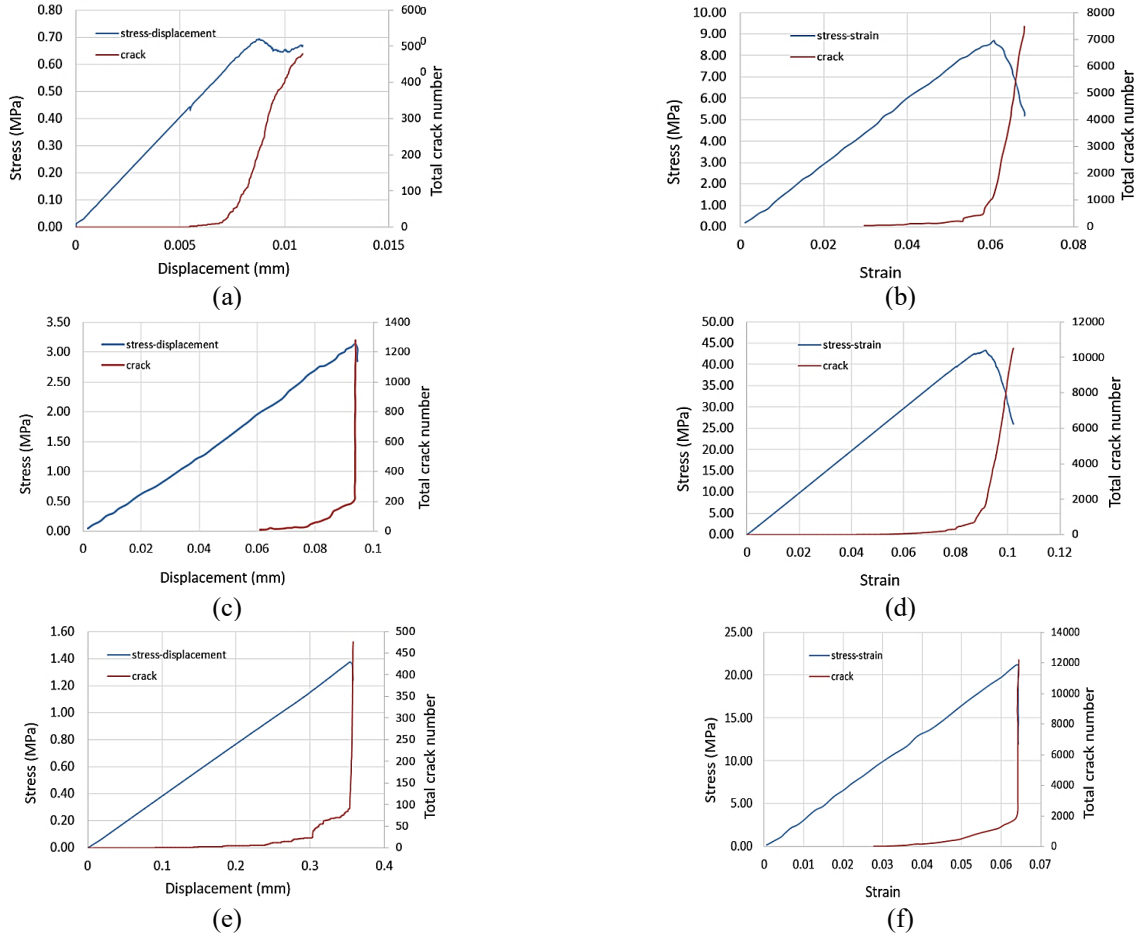

Fig. 10 (a) Stress vs. axial displacement and total crack count for gypsum, (b) For gypsum, the ratio of axial compression stress to axial strain and the total number of cracks, (c) For hard concrete, stress relative axial displacement and total crack count, (d) For hard concrete, the ratio of axial compression stress to axial strain and the total number of cracks. (e) for weak concrete, stress vs axial displacement and total crack count and (f) For weak concrete, the ratio of axial compression stress to axial strain and the number of fractures overall

and 0.1 MPa respectively. The particle bonding strengths are 0.5 MPa for gypsum, 15 MPa for high-strength concrete, and 10 MPa for low-strength concrete, with cohesion standard deviations of 0.05 MPa, 1.5 MPa, and 1 MPa accordingly. All materials have a porosity of 0.08 and consist of 2 components each. Lastly, the ratio of shear stiffness to normal stiffness (Kn/Ks) is 1.7 for gypsum and low-strength concrete, and 1.9 for high-strength concrete.

Gypsum and concrete both have a specified diameter of 54 mm for such Brazilian examination that PFC2D modeled. Gypsum's regular dimensions for the uniaxial test that PFC2D simulates are 54 mm in length and 108 mm in depth, whereas concrete's normal measurements are 150 mm in length and 150 mm in height. A standardized velocity of 0.016 m/s is used to move the sample's top and bottom two walls toward one another. Figs. depict the results of the numerical compressive strength test for concrete as well as gypsum. 9. One may get the conclusion that there is a clear correlation and resemblance seen between experiments conducted and numerical modeling of geo-materials by comparing Figs. 9 and 2 to each other.

Figs. 8(a), 8(c) and 8(e) show the tensile stress curve versus axial displacement along with total crack number for gypsum, hard concrete and weak concrete models. Also, Figs. 8(a) and 8(b) illustrate the axial compressive stress curve versus axial strain along with total crack number for gypsum, hard concrete and weak concrete models. These curves are similar with the typical diagram of experimental tests.

Table 2 lists the tensile strength and strength properties values that were determined by the numerical testing. These numerical values, which are listed in Table 1, are quite near to those experimentally observed values. The models are therefore appropriately calibrated for PFC2D.

3.2 Blasting simulation

The interlayer is frequently seen in real blasting engineering. The quality and effect of blasting are frequently greatly influenced by the position, thickness, and persistency of the interlayer. This leads to the single-hole blasting tests that are conducted in this study at various locations, persistencies, and various thicknesses of both the hard concrete and the weak gypsum interlayer. This same single-hole blasting parametric study (Tables 3-5) is made up based on the particle flow code (PFC2D), with a scale of

Table 3 Numerical model with gypsum interlayer length of 6000 mm

Distance between central hole and gypsum interlayer (b) (mm)	Interlayer thickness (a) (mm)		
	450	300	150
900	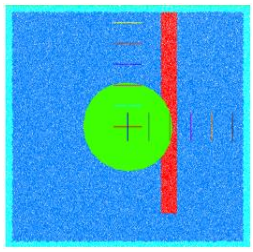	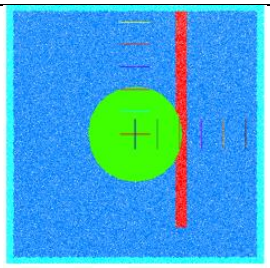	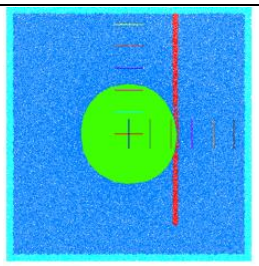
1500	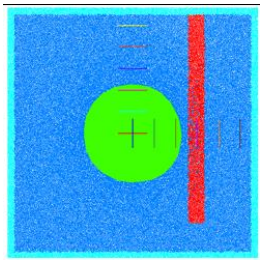	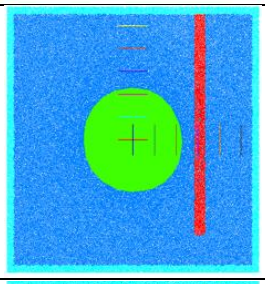	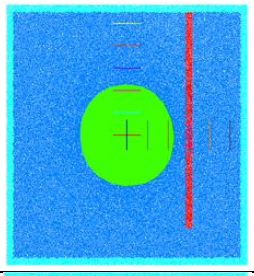
2100	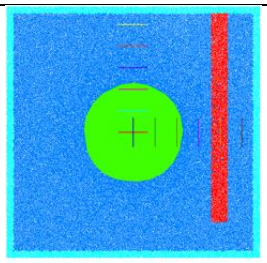	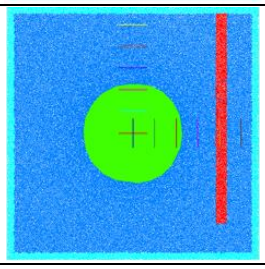	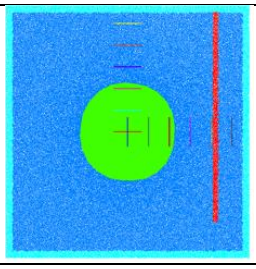

7000 mm * 7000 mm. The blasting hole measured 100 mm in diameter. The explosion point becomes reduced to a 50 mm diameter particle that is placed in the model's middle. Somewhere on the right side of something like the blast hole, there was one interlayer. Tables 3 until Table 5 illustrate the unique interlayer distribution instances. To track the peak stress Sxx, two stress measuring circles are positioned mostly on the left and right sides of either the weak interlayer (Table 6). Additionally, measurement walls were placed in the the X and Y axes to track the Sxx and Syy at various distances from the hole center; namely, 0, 600 mm, 1200 mm, 1800 mm, 2400 mm, and 3000 mm (Table 6). Elements have circle shape because simulation was performed in two dimension. Totally 1956 discs were used to make the packing model with porosity of 0.08.

In order to prevent stress waves from reflecting off the boundary, this study addresses the fluid boundary presented by Kouroussis *et al.* (2011) and Zhou *et al*. (2000) as well as the dispersion influence of stress wave propagation someplace at the rock mass barrier (Table 6). The blasting load is applied using the blasting point expansion technique (Zhou 2020). The expanding explosion point particle will engulf nearby rock mass particles as it grows. Each model was simulated nearly in 2 hours due to dynamic condition stabilization. The circumferential force F on the nearby rock particles following explosion point growth is as follows, in accordance with the particle interaction principle of PFC

$$F = K_n\, d = 2\pi r_0 p \tag{2}$$

The particle expansion radius of the explosion location is then

$$d = \frac{2\pi r_0 p}{K_n} \tag{3}$$

Where r_0 is the blast point's beginning radius, d is the blast point's circumference after expanding, p is the stress mostly on the rock wall, K_n is the particle interaction stiffness, and r_0 is the blast point's radius in fact. The explosion load distributes to the neighboring rock mass from the explosion site, and the motion resembles a pulse wave. It may be represented as a half sine wave (also described as an ordinary least square curve) at the same time with both the rising and the falling regions, as seen in Fig. 11.

$$d = \frac{p}{2}\left(1 - cos\left(\frac{2\pi}{\Delta T}t\right)\right) \tag{4}$$

Where $\triangle$T is the half-time of an oscillatory operation, which is typically 10 ms, p is the maximum pressure in the hole, p(t) seems to be the blasting load upon that hole wall, and t is indeed the length of time, which is 20 ms.

The Mohr-Coulomb criterion was selected to forecast the initiation and growth of cracks. Cohesion and friction

Table 4 Numerical model with gypsum interlayer length of 4000 mm

Distance between central hole and gypsum interlayer (b) (mm)	Interlayer thickness (a) (mm)		
	450	300	150
900	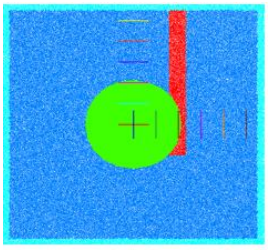	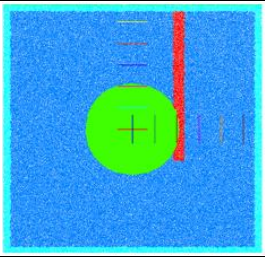	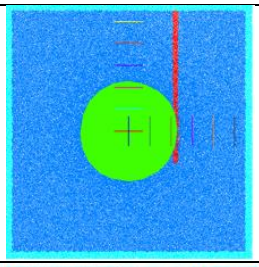
1500	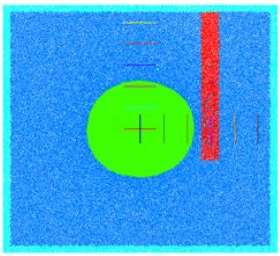	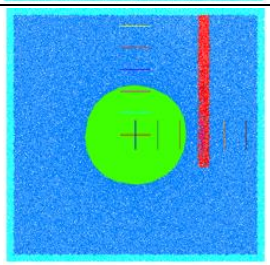	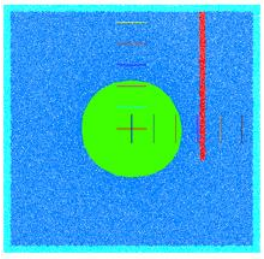
2100	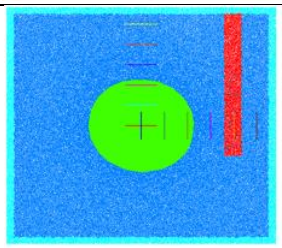	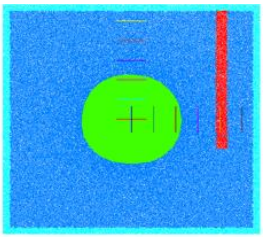	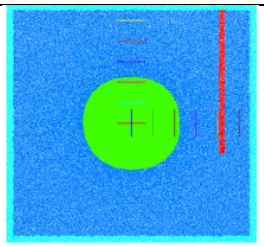

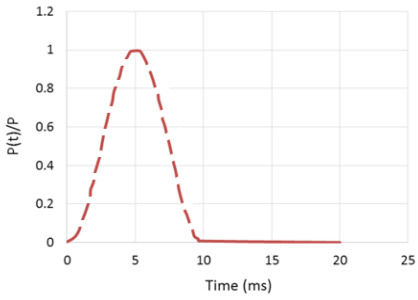

Fig. 11 Curve of blast pressure load history

angles are the two primary parameters associated with this criterion. When the shear stress between particles reaches the shear strength, a shear crack is triggered in the model. Conversely, when the tensile stress between particles attains the tensile strength, a tensile crack is generated in the model.

3.3 Numerical simulation results

3.4.1 Failure pattern

a)Soft interlayer

Tables 14-16 show the failure pattern of numerical model. Tensile crack and shear crack were depicted by black line and yellow line, respectively. Totally, tensile cracks were developed perpendicular to blasting hole while shear cracks were developed perpendicular to tensile crack direction. It is important to note that the soft interlayer is where both the tensile crack and even the shear crack occurred. The number of cracks decreased, rather than their length, as the distance increased between the central hole and the gypsum interlayer. The shape of the cracks changed significantly with a constant interlayer thickness and a spacing of about 1500 mm from either blast hole. The main indicators of crack changes in the soft interlayer are the lateral expansion of cracks and the widening of the crushing surface as the distance increases. The significant stress wave absorption in soft rock minimally affects the surrounding concrete, demonstrating how effectively the weak interlayer dissipates blasting energy to prevent stress wave transmission. The two main signs of a crack change in host concrete are an increase in blast hole rock damage and a weak interlayer. The primary fracture keeps growing because the stress wave is transmitted by that of the structural plane and is blocked by the crack, which keeps the left side of the host concrete foundation from being impacted by the weak interlayer. The amount of fractures increases and the final state changes when the thickness of either weak interlayer increases after the space (b) between the weak interlayer and the blast hole is established. The number of fractures, the extent of the expansion, and the level of damage are mostly dramatically rising in the host

Table 5 Numerical model with gypsum interlayer length of 2000 mm

Distance between central hole and gypsum interlayer (b) (mm)	Interlayer thickness (a) (mm)		
	450	300	150
900	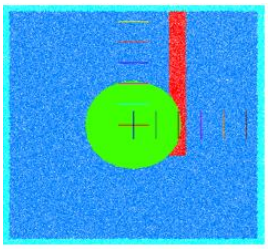	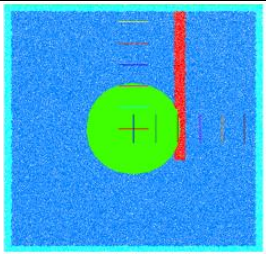	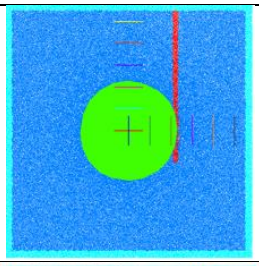
1500	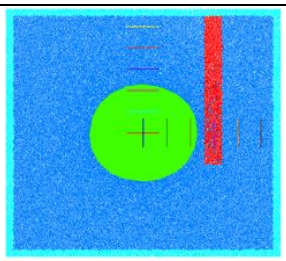	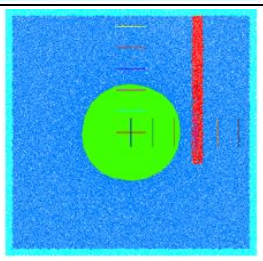	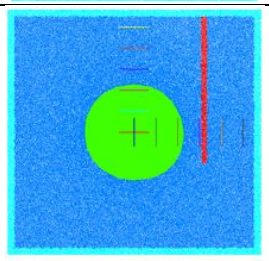
2100	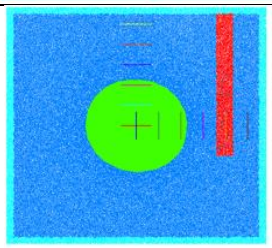	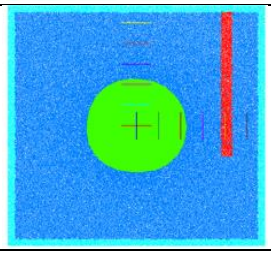	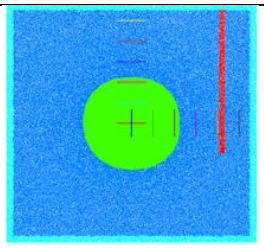

concrete. According to this, the host concrete around the blast hole as well as the weak interlayer would sustain more severe damage the stronger the restricted interlayer, which will reflect a greater amount of stress waves. With increasing interlayer thickness in soft interlayers, the crack initiation spectrum becomes considerably wider. Also because a soft interlayer can withstand the entirety of the blasting energy, there are basically no cracks within the host concrete simply on the right side of a layer that resembles an interlayer. With both the thickness of either the weak interlayer, there is no question that the amount of damage to the concrete around blast holes increases. When the thickness of the weak interlayer remains the same and the distance from the blast hole exceeds 1500 mm, the frequency of fractures decreases as the gap between the core hole and the gypsum interlayer increases, while crack propagation largely stays constant. This shows that when the weak interlayer is outside the fragmentation zone, increased distance reduces both the reflected stress wave and energy transfer, preventing further crack expansion and resulting in less damage to surrounding concrete. As the gap widens, fractures in the soft interlayer are significantly reduced, leading to fewer and shorter-duration breaks in the weak interlayer. Additionally, if the distance from the blast hole increases while the interlayer thickness remains constant, the soft interlayer sustains severe damage before the concrete cracks. The reduced strength of the gypsum interlayer in comparison to the concrete's base material is what causes this. Comparisons comparing Tables 7-9 reveal that when the interlayer lengthens, the length as well as frequency of cracks greatly increase, and indeed the fracture shape significantly changes. As the interlayer length increases, the crack alteration within the soft interlayer is mostly observed as an extension of the fracture in a transverse direction but also an enhancement in the crushing area. Large amounts of stress wave consumption in the soft interlayer have little to no direct impact on the hard concrete, which also shows that a weak interlayer might actually immediately and dramatically decrease the energy produced by blasting in order to stop stress wave propagation. The main signs of a crack change in hard concrete are an increase in blast hole rock damage and a weak interlayer. The primary fracture keeps growing because the stress wave is reflected by the structural plane and is blocked by the crack, even if the weak interlayer has no effect on the host concrete foundation's left side of either blast hole.

b) Hard interlayer

Tables 17-19 show the failure pattern of numerical model with hard interlayer. Tensile crack and shear crack were depicted by black line and yellow line, respectively. Totally, tensile cracks were developed perpendicular to blasting hole while shear cracks were developed perpendicular to tensile crack direction. Its to be note that only tensile crack was developed through the hard interlayer.

Table 6 Different configuration of soft and hard interlayer

Case	Distance between central hole and gypsum interlayer (b) (mm)	Interlayer length (c) (mm)	interlayer thickness (a) (mm)	Model shape
1	900	2000	150	
2	900	2000	300	
3	900	2000	450	
4	900	4000	150	
5	900	4000	300	
6	900	4000	450	
7	900	6000	150	
8	900	6000	300	
9	900	6000	450	
10	1500	2000	150	
11	1500	2000	300	
12	1500	2000	450	
13	1500	4000	150	
14	1500	4000	300	
15	1500	4000	450	
16	1500	6000	150	
17	1500	6000	300	
18	1500	6000	450	
19	2100	2000	150	
20	2100	2000	300	
21	2100	2000	450	
22	2100	4000	150	
23	2100	4000	300	
24	2100	4000	450	
25	2100	6000	150	
26	2100	6000	300	
27	2100	6000	450	

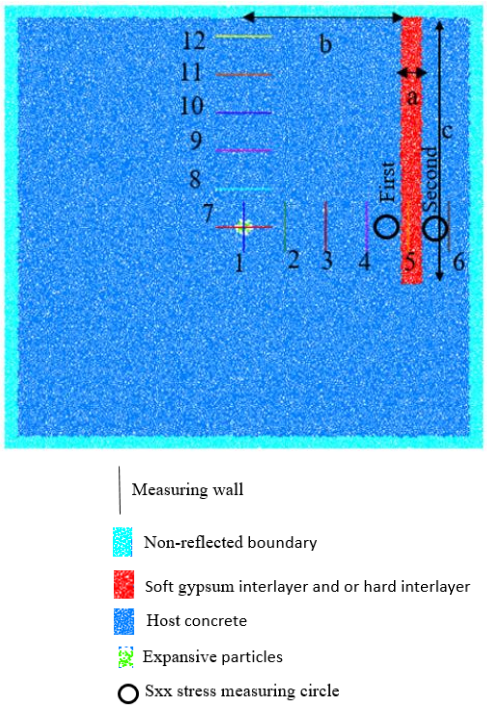

This same length and number of crack formations decreased with an increase in distance between the central hole and the hard concrete interlayer when the thickness of the hard interlayer was constant and the distance from the blast hole became less than around 2100 mm (three times greater than the radius of the crushing area). The crack shape also changed significantly. The existence of a hard interlayer causes the crushing area to decrease as the separation between both the interlayer and also the blast hole increases. The host concrete somewhat on the correct side of the interlayer is severely impacted by the minimal amount of stress wave consumption in the hard interlayer, demonstrating further that the hard interlayer is unable to minimize blasting energy in order to aid in stress wave propagation. The major fracture extended farther on the right side of such a hard interlayer as a result of stress wave amplification by the interlayer and stress wave movement. The number of fractures reduces when the hard interlayer's thickness is increased whenever the distance (b) separating it from the blast hole is known. The host concrete's number of cracks, expansion range, and degree of damage around the blast hole have all decreased. This indicates that the harder the hard interlayer, therefore more effective refractive stress waves it will cause, which will lead to very little destruction to the host concrete around the blast hole and indeed the hard interlayer. It is seen in the hard interlayer that the fracture propagation range decreases as the hard interlayer's thickness increases. The majority of the blasting energy can pass through the tough interlayer, causing fissures in the host concrete on the right side of either interlayer. The amount of host concrete damage surrounding blast holes decreases with an increase in the hard interlayer's thickness. When the hard interlayer's thickness remained constant as well as the distance from the blast hole was greater than 2100 mm, the frequency of cracks increased as the distance from the center hole to the gypsum interlayer grew. The hard interlayer's presence in the crushing zone shows that as the distance from the central hole increases, the refractive stress wave strengthens, causing energy buildup between the blast hole and structural plane. This leads to the original fracture extending and more damage to the surrounding concrete. With a greater gap, the stress wave's diffusion to the interlayer weakens, significantly reducing crack formation in the hard interlayer. Consequently, both the quantity and length of the cracks decrease, similar to when the distance between the hard interlayer and blast hole is constant while the weak interlayer's thickness increases, resulting in more fractures. It is clear from a comparison of Tables 10, 11, and 12 that as the interlayer length increases, so does the length as well as the number of cracks, and that the crack morphology also dramatically alters.

Table 7 Failure pattern of numerical model; gypsum interlayer length=6000 mm

Distance between central hole and gypsum interlayer (b) (mm)	Gypsum interlayer thickness (a) (mm)		
	150	300	450
900	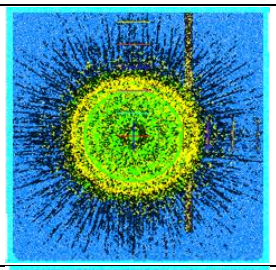	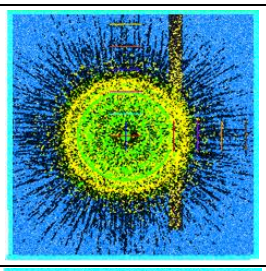	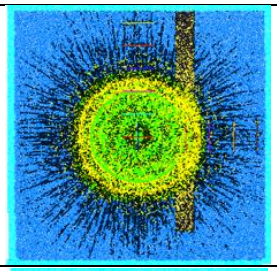
1500	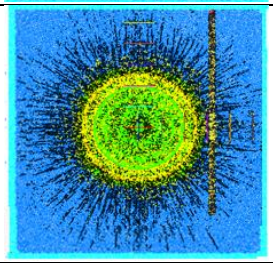	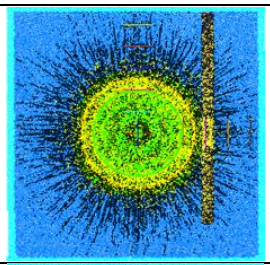	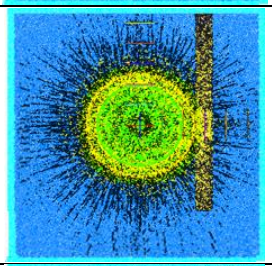
2100	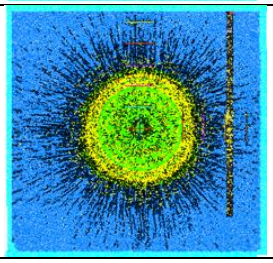	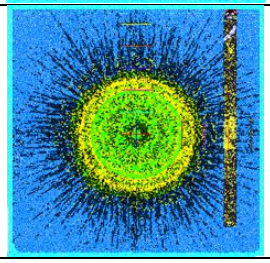	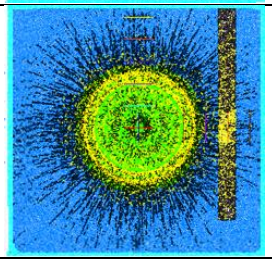

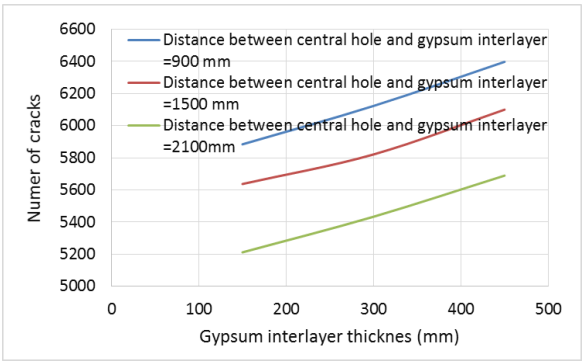

(a)

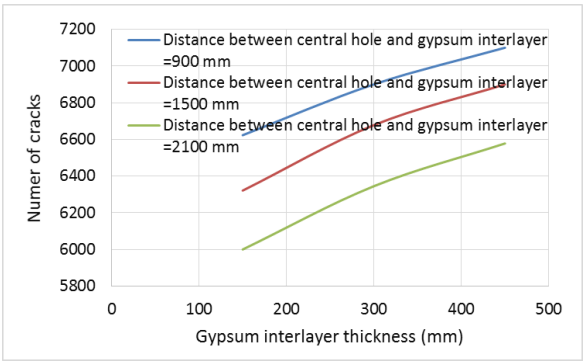

(b)

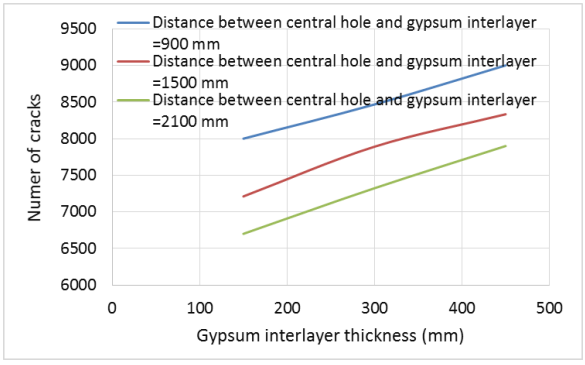

(c)

Fig. 12 variation in crack numbers for interlayer lengths of (a) 2000 mm, (b) 4000 mm, and (c) 6000 mm, influenced by the weak interlayer thickness and spacing from the blast hole

Table 8 Failure pattern of numerical model; gypsum interlayer length=4000 mm

Distance between central hole and gypsum interlayer (b) (mm)	Gypsum interlayer thickness (a) (mm)		
	150	300	450
900	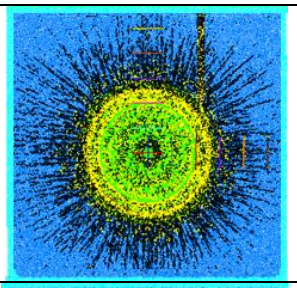	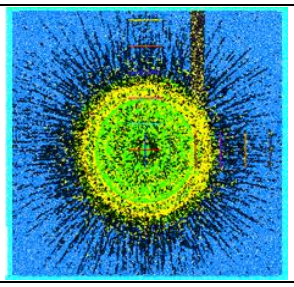	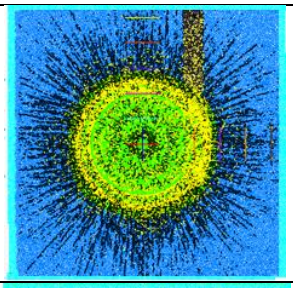
1500	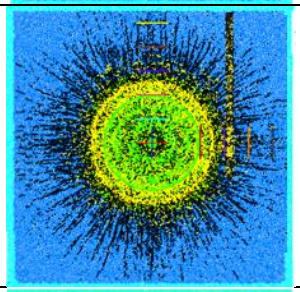	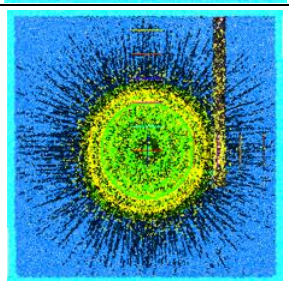	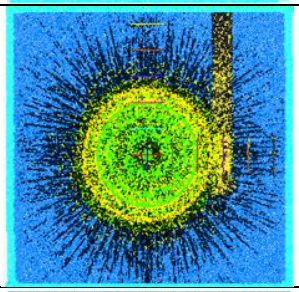
2100	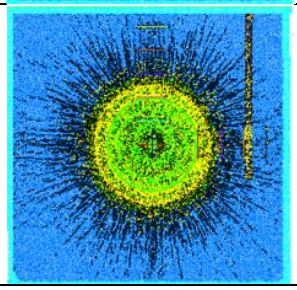	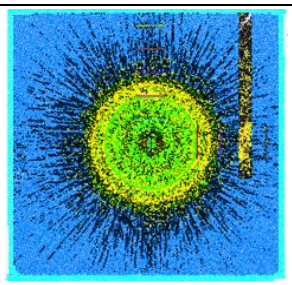	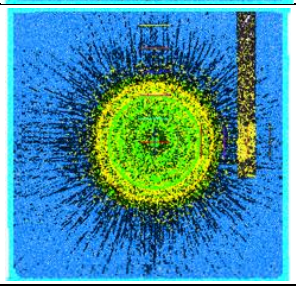

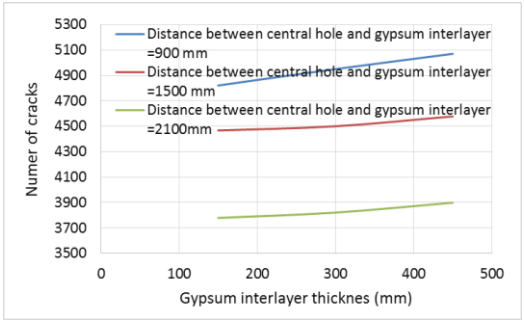

(a)

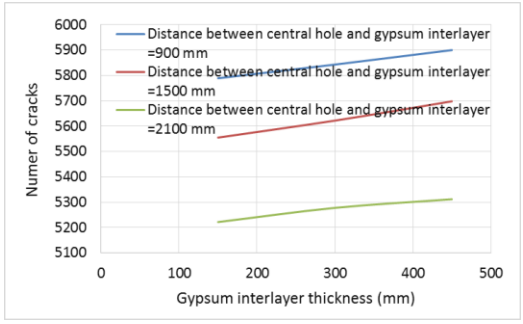

(b)

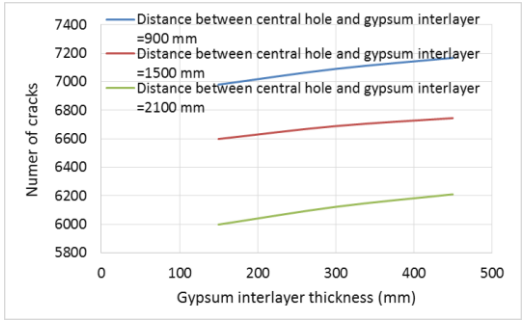

(c)

Fig. 13 Based on the thickness of something like the weak interlayer and thus the separation between the strong interlayer and indeed the blast hole, crack numbers vary for three different interlayer lengths of 2000 mm, 4000 mm, and 6000 mm

Table 9 Failure pattern of numerical model; gypsum interlayer length=2000 mm

Distance between central hole and gypsum interlayer (b) (mm)	Gypsum interlayer thickness (a) (mm)		
	450	300	150
900	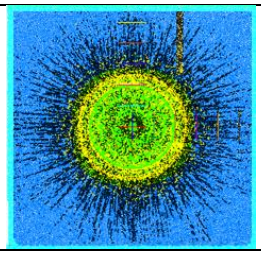	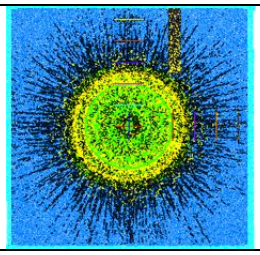	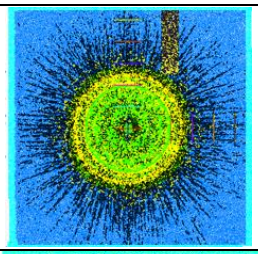
1500	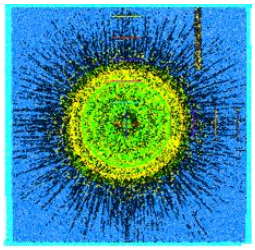	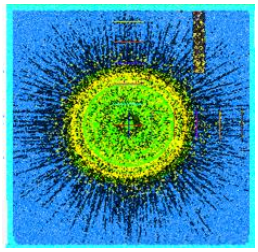	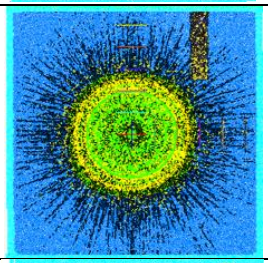
2100	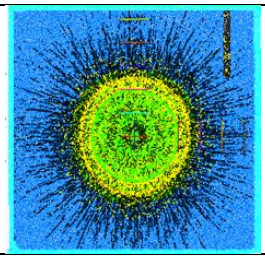	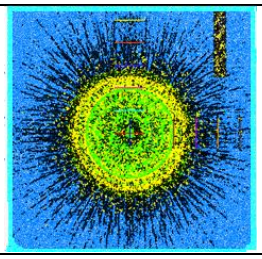	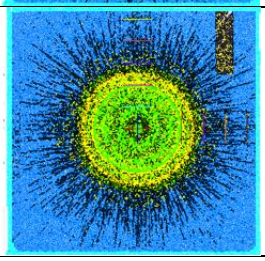

When there is a hard interlayer present, the crushing area decreases as the interlayer length increases. The host concrete somewhat on right side of the interlayer is damaged because the hard interlayer does not consume as much stress wave energy, demonstrating that it is unable to shift the stress wave's propagation. When blast holes and weak interlayers cause more rock damage in the host concrete, cracks start to appear more often. The major fracture extended farther on the correct side of a hard interlayer as a result of stress wave dispersion by the interlayer and stress wave movement.

3.3.2 Blasting crack number

a)soft interlayer

In accordance with the thickness of the soft interlayer, Figs. 12(a)12(c) depicts the development curve of fracture number for three various interlayer lengths, namely 2000 mm, 4000 mm, and 6000 mm. As the thickness of both the weak interlayer grows, the number of fractures also rises consistently. Gypsum interlayer thickness had no impact on the frequency of cracks when the distance between the central hole and the interlayer was 2100 mm (Fig. 12(a)) when such interlayer length measured 2000 mm. This is caused by wave dampening before it reaches the weak interlayer and the vast interval between the center hole and gypsum interlayer.

b) hard interlayer

In accordance with the thickness of the hard interlayer, Figs. 13(a)-13(c) depicts the development curve of the crack number for three separate interlayer lengths, namely 2000 mm, 4000 mm, and 6000 mm. As the thickness of either the weak interlayer grows, the number of fractures also rises consistently. It may be inferred from Figs. 13 and 12 that there were fewer overall fractures in the hard interlayer than in the soft interlayer. The increasing rate of crack number with interlayer thickness in soft interlayer is more than that in hard interlayer. Also, crack numbers were decreased by increasing the distance between the central hole and interlayer. The decreasing rate in hard interlayer (vertical distance between the blue, red and green lines) was more than that in soft interlayer.

3.3.3 Different stress levels on the interlayer's opposing surfaces

a)soft interface

To track the peak stress Sxx, the initial and subsequent actions points are positioned mostly on the left and right sides of the interlayer (Table 6). The weak interlayer's distance from the blast hole and the variation curve of Sxx are derived (Fig. 14). As seen in Figs. 14(a), 14(c), and 14(e), Sxx has a significantly declining trend with b <1500. As the interval between the blast hole and the plane of a structure increases, the attenuation tendency of the curve slows and becomes more stable. Together with the fracture results, Tables 7-9 demonstrate that whenever the soft interlayer becomes thin, the hard concrete will experience

Table 10 Failure pattern of numerical model; concrete interlayer length=6000 mm

Distance between central hole and gypsum interlayer (b) (mm)	concrete interlayer thickness (a) (mm)		
	150	300	450
900	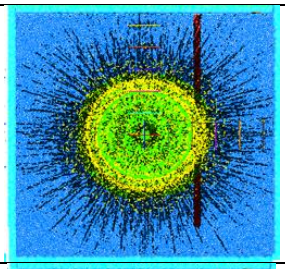	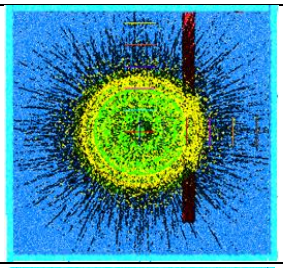	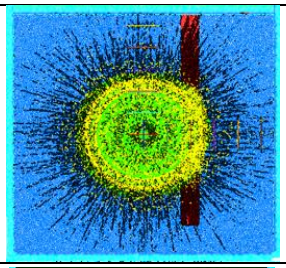
1500	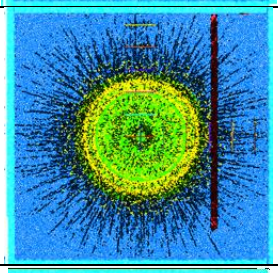	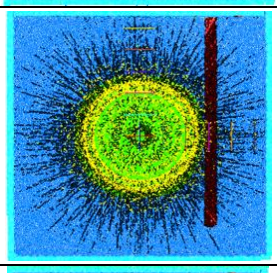	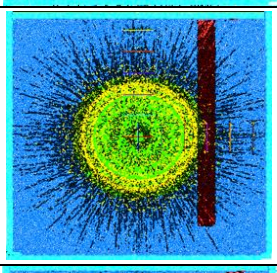
2100	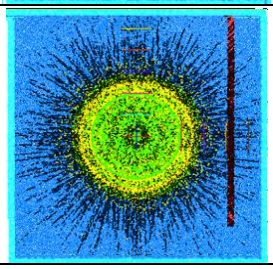	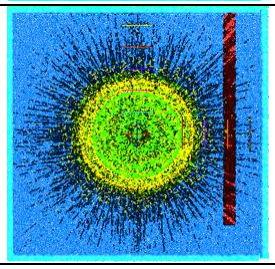	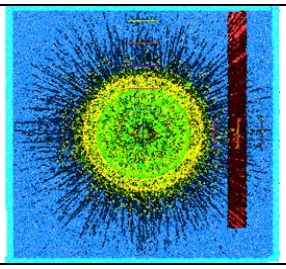

large levels of stress due to the soft gypsum's damage from the stress wave on both sides. The stress on both sides of the concrete is larger and the degree of damage to the hard concrete is greater the thinner the soft interlayer is. Sxx exhibits a declining trend as blast hole and interlayer distance rise provided interlayer thickness is constant. The stress wave progressively weakens in the dense concrete as the interlayer moves closer to the blast hole, leading to a significant accumulation of stress in the concrete specimen located between the blast hole and the interlayer. In contrast, when the interlayer is far from the blast hole (b > 1500 mm), the stress value in that segment of the curve is relatively low, the attenuation of the stress wave is notable, and the stress wave associated with the interlayer struggles to converge within the dense concrete located between the blast hole and the interlayer. Increasing the thickness of the interlayer resulted in a reduction of Sxx. A comparison of Figs. 14(a), 14(c), and 14(e) indicates that Sxx increased when the interlayer was shortened. The extension of the interlayer's length led to greater stress attenuation. When the length of such soft interlayers exceeded 6000 mm (referencing Figs. 14(e) and 14(f), the hard concrete experienced high-stress conditions due to damage from the stress wave of the soft rock being transmitted to it from both sides. There is an inverse relationship between the length of the soft interlayer and the stress experienced by the concrete, as well as the extent of damage to the hard concrete.

Additionally, Sxx exhibits an overall declining trend as the distance from the blast hole to the structural plane increases, as illustrated in Figs. 14(b), 14(d), and 14(f), and the overall pattern of the curve aligns closely with Figs. 14(a), 14(c), and 14(e). This holds true even when the thickness of the weak interlayer remains unchanged. When the weak interlayer is beyond the four-fold crushing area, the Sxx values of the concrete on both sides are relatively low and nearly stable, with Sxx decreasing gradually as the distance between the blast hole and the structural plane increases. It should be highlighted that the second measuring circle may have undergone greater stress attenuation compared to the first.

b) Hard interface

Sxx exhibits a significantly declining trend including all distances seen between hard interlayers but also blasting holes, as seen in Figs. 15(a), 15(c), and 15(e). As the separation between blast holes and the structural plane increases, the absorption trend of something like the curve becomes more stable. Tables 10 through 12 together with the crack findings demonstrate that when the hard interlayer is thin, the low-stress wave damage of the hard interlayer will be communicated to the host concrete on either side, putting the host concrete in a high-stress condition. The host concrete is subjected to greater stress and is subjected to more damage on both sides of the thicker underlying hard interlayer. Sxx exhibits a declining trend as blast hole and

Table 11 Failure pattern of numerical model; concrete interlayer length=4000 mm

Distance between central hole and gypsum interlayer (b) (mm)	concrete interlayer thickness (a) (mm)		
	150	300	450
900	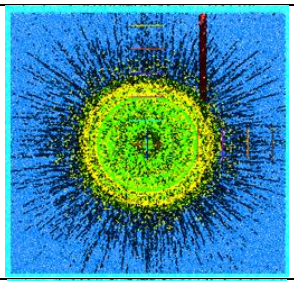	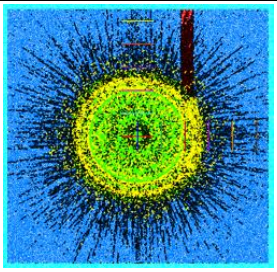	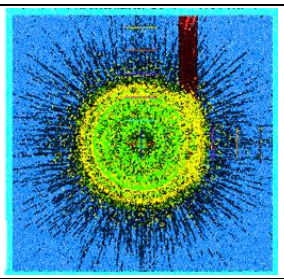
1500	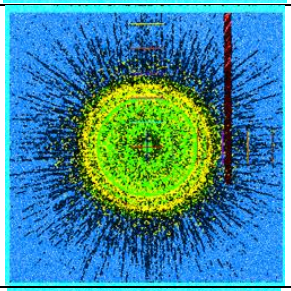	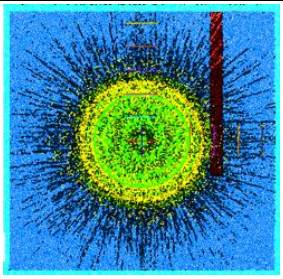	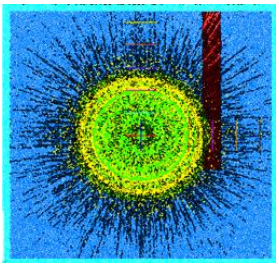
2100	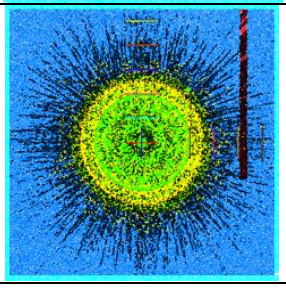	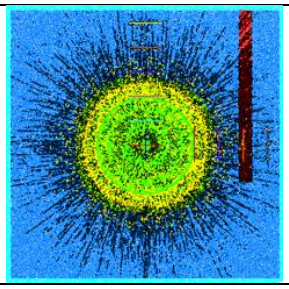	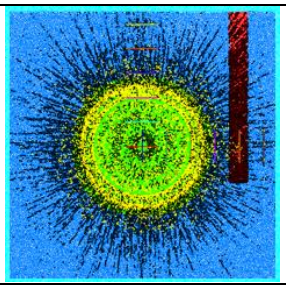

interlayer distance rise assuming interlayer thickness is constant. The stress wave decreases in the surrounding concrete as the interlayer moves further from the blast hole, leading to a higher applied load in that segment of the curve. When the interlayer is far from the blast hole, the stress wave's retardation amplitude is significant, and the wave is refracted by the interlayer in the host concrete, resulting in a relatively high ultimate load for that portion of the curve. By thickening the interlayer, Sxx was reduced. It is clear from a comparison of Figs. 15(a), 15(c) and 15(e) that lengthening the interlayer increased Sxx. Reducing the interlayer length reduced the stress attenuation. The hard concrete is in a high-stress condition when the hard interlayer length is more than 6000 mm (Figs. 15(e) and 15(f)). This is because less damage to the hard interlayer from stress waves will be communicated to the host concrete on both sides. The tension on the host concrete and the degree of damage to the host concrete increase as the hard interlayer length decreases.

Additionally, Sxx has a general decreasing tendency as the separation between blast holes as well as the structural plane increases, as illustrated in Figs. 15(b), 15(d) and 15(f), and the common rule of curves are essentially identical with Figs. 15(a), 15(c) and 15(e). It should be noted that the stress absorption was greater in the second measurement circle than it was in the first.

3.3.4 Evolution of energy fields

This research investigates the blasting findings from the perspectives of kinetic energy, friction energy, and strain energy in order to investigate the impact of the location, length, and thickness of interlayer on concrete energy.

a) Soft interlayer

a)Interlayer length was 6000 mm

The connection among vertex kinetic energy, vertex friction energy, peak strain energy, and the distance from the blast hole to the structural plane is illustrated in Figs. 16(a)-16(c). These results were presented with three different interlayer thicknesses. The peak kinetic energy and the maximum friction energy of concrete structures can be divided into two segments as the distance from the blast hole to the structural plane increases, as shown in Figs. 16(a) and 16(b), provided the interlayer thickness remains unchanged. The rapid decline section is evident when the distance from the blast distance is less than 1500 mm, changes in the weak interlayer thickness have the most significant effect on both the kinetic energy peak and the friction energy peak. After calculations, the kinetic energy peak and friction energy peak are projected to increase by approximately 21% and 12%, respectively, with thickness increases in this range. The curvature of the slow descent phase occurs when the positions of the weak interlayer and

Table 12 Failure pattern of numerical model; concrete interlayer length=2000 mm

Distance between central hole and gypsum interlayer (b) (mm)	concrete interlayer thickness (a) (mm)		
	450	300	150
900	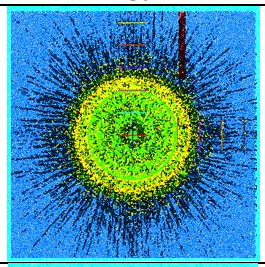	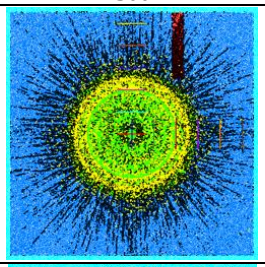	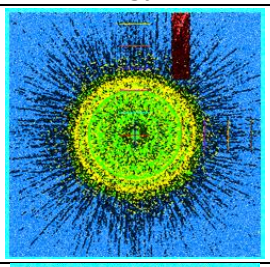
1500	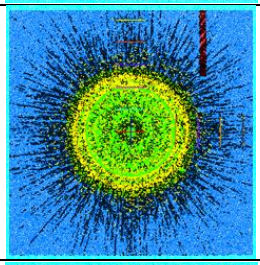	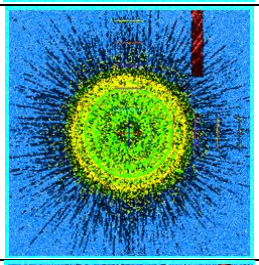	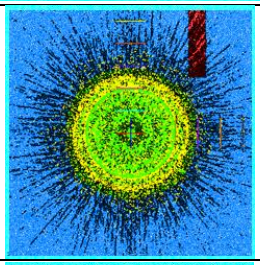
2100	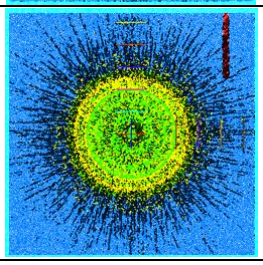	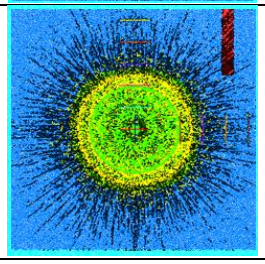	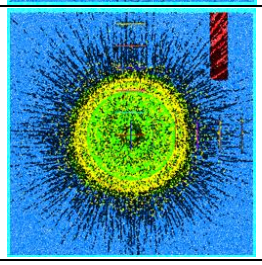

the blast hole are fixed and are not within the fourfold crushing zone. The alterations in the distance from the blast hole to the structural plane, as well as the thickness of the interlayer, have a negligible effect on both the peak kinetic energy and the friction energy within this range, with the changes in the two peaks remaining mostly stable. When the thickness of the interlayer appears to be constant, as shown in Fig. 14(c), it is clear that the overall peak strain energy increases as the distance between the blast hole and the structural plane grows. The distribution of peak strain energy can be divided into two segments based on the amplitude of fluctuations. When the distance between the structural plane and the blast hole is less than 1500 mm, the peak strain energy increases rapidly with rising b. If the distance exceeds 1500 mm, the resonance frequency of strain energy stabilizes, although changes remain minimal. The variation in strain energy (from b = 0.0 m to b = 1500 mm) grows with thicker weak interlayers when both are within twice the crushing area. A decrease in interlayer thickness is expected to raise peak strain energy by about 208 kJ. Beyond the fourfold crushing area, the peak strain energy change stays modest at around 2820 kJ, remaining stable despite variations in distance or interlayer thickness.

b) Interlayer length=4000 mm and 2000 mm

The fluctuation of energy against the separation between the blast hole and the structural plane assuming interlayer lengths of 4,000 mm and 2000 mm, respectively, is depicted in Figs. 17 and 18. It is clear from a comparison of Figs. 16 to 18 that shortening the interlayer length reduced both the kinetic energy peak and the friction energy peak. The interlayer length was shortened, which increased strain energy.

The wave propagation during blasting decreased with more interfaces. As the interface dip angle increased, wave attenuation decreased.

b) Hard interlayer

a)Interlayer length was 6000 mm

The relationship between vertex kinetic energy, vertex friction energy, vertex strain energy, and the separation between both the structural line and the explosion hole is depicted in Figs. 19(a)-19(c). Three alternative interlayer thicknesses were shown with these results. As shown in Figs. 19(a) and 19(b), whenever the separation seen between blast hole and even the structural surface is less than 2100 mm, both the peak kinetic energy and peak friction energy decrease as the difference in separation between the two (b2100). The values of these two curves also drop collectively when the thickness of the weak interlayer increases for every point of the hard interlayer examined in this study. Modifications in the hard interlayer thickness at closer ranges have a greater impact on friction energy peaks than kinetic energy peaks. After calculation, the kinetic energy maximum and friction energy high within

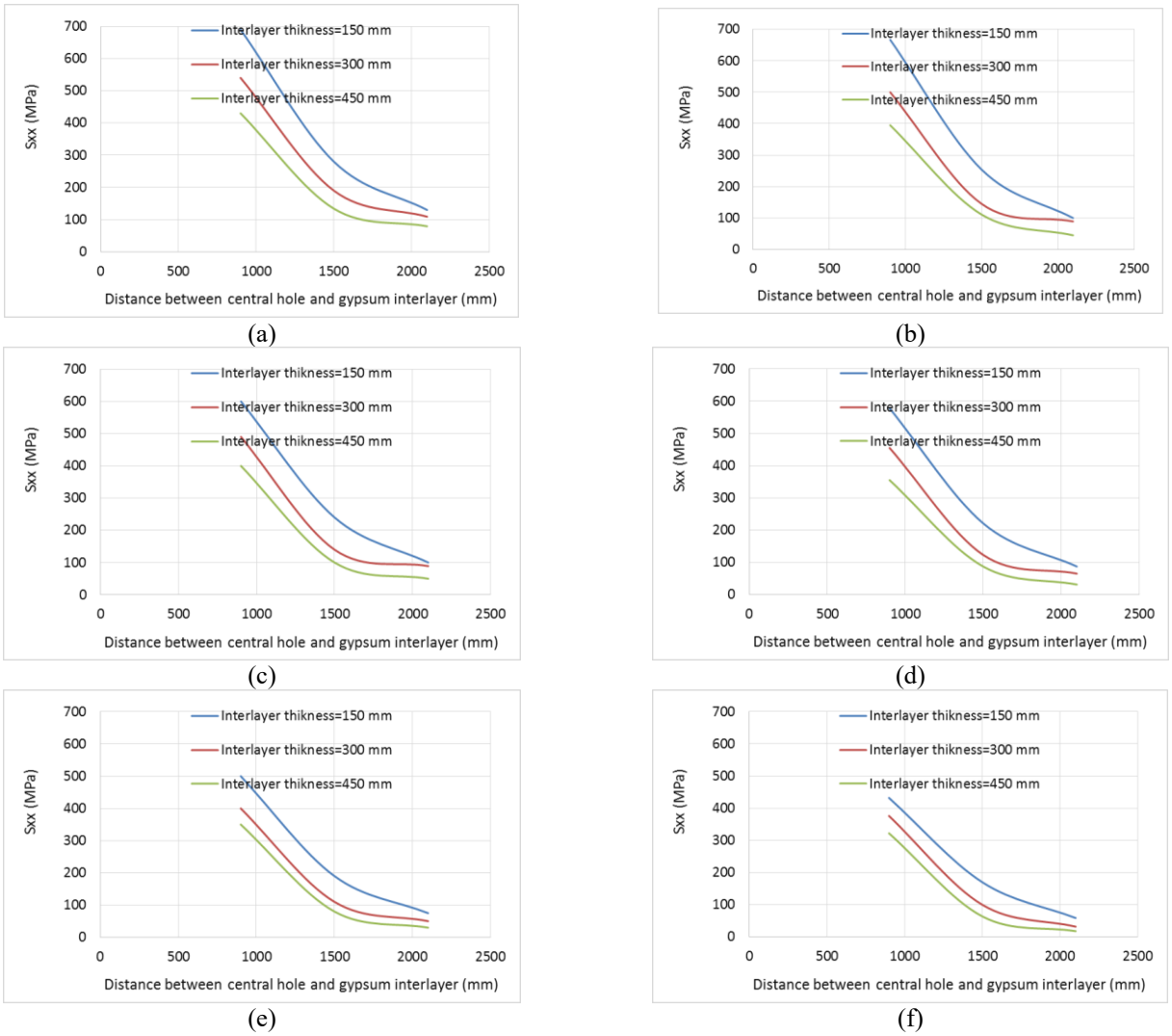

Fig. 14 Variation of Sxx for three distinct interlayer lengths of (a) 2000 mm, (b) 4000 mm, and (c) 6000 mm depending on the the weak interlayer's thickness and the spacing between it and the blast hole

this domain will decrease by about 18% and 10% of the content increase, respectively. As observed in Fig. 19(c), when the hard interlayer thickness has been fixed, the peak strain energy rises overall as the distance between the blast hole and with structural plane increases. According to calculations, an increase in interlayer thickness will result in a peak strain energy increase of roughly 290 kJ.

b) Interlayer length=4000 mm and 2000 mm

The fluctuation of energy against the separation between the blast hole and the structural plane assuming interlayer lengths of 4,000 mm and 2000 mm, respectively, is depicted in Figs. 20 and 21. It is clear from a comparison of Figs. 19 to 21 that lengthening the interlayer lowered both the kinetic energy peak and also the highest frictional energy. The interlayer length was lengthened, which increased strain energy. This results from the hard interlayer's impact on the model's wave refraction.

It may be inferred from a comparison of Figs. 18 and 19 that the kinetic energy peak, as well as friction energy peak throughout the soft interlayer model, were higher than those in the hard interlayer model. Additionally, it can be deduced from a comparison of Figs. 18 and 19 that now the strain energy peak inside this soft interlayer type was lower than that in the hard interlayer model. This is because the host concrete's soft interlayer has a significant impact on dampening wave propagation.

3.3.5 Variation of the pressures at different distances from hole center in both of the X and Y axes in concrete interlayer and gypsum interlayer

Figs. 22(a) and 22(b) show the variation of the pressure at different distances from hole center in both of the X and Y axes for concrete interlayer and gypsum interlayer, respectively. These values were presented for a=450 mm, b=900 mm and c= 6000 mm. Both of the Sxx and Syy was decreased by increasing the distance from hole center. In all cases, the Syy was more than Sxx. In the case of gypsum interlayer, pressure in x direction was less than that in case of concrete interlayer. This is due to stress attenuation due to presence of gypsum interlayer. Similar results was obtained for other interlayer lengths, thicknesses and distances.

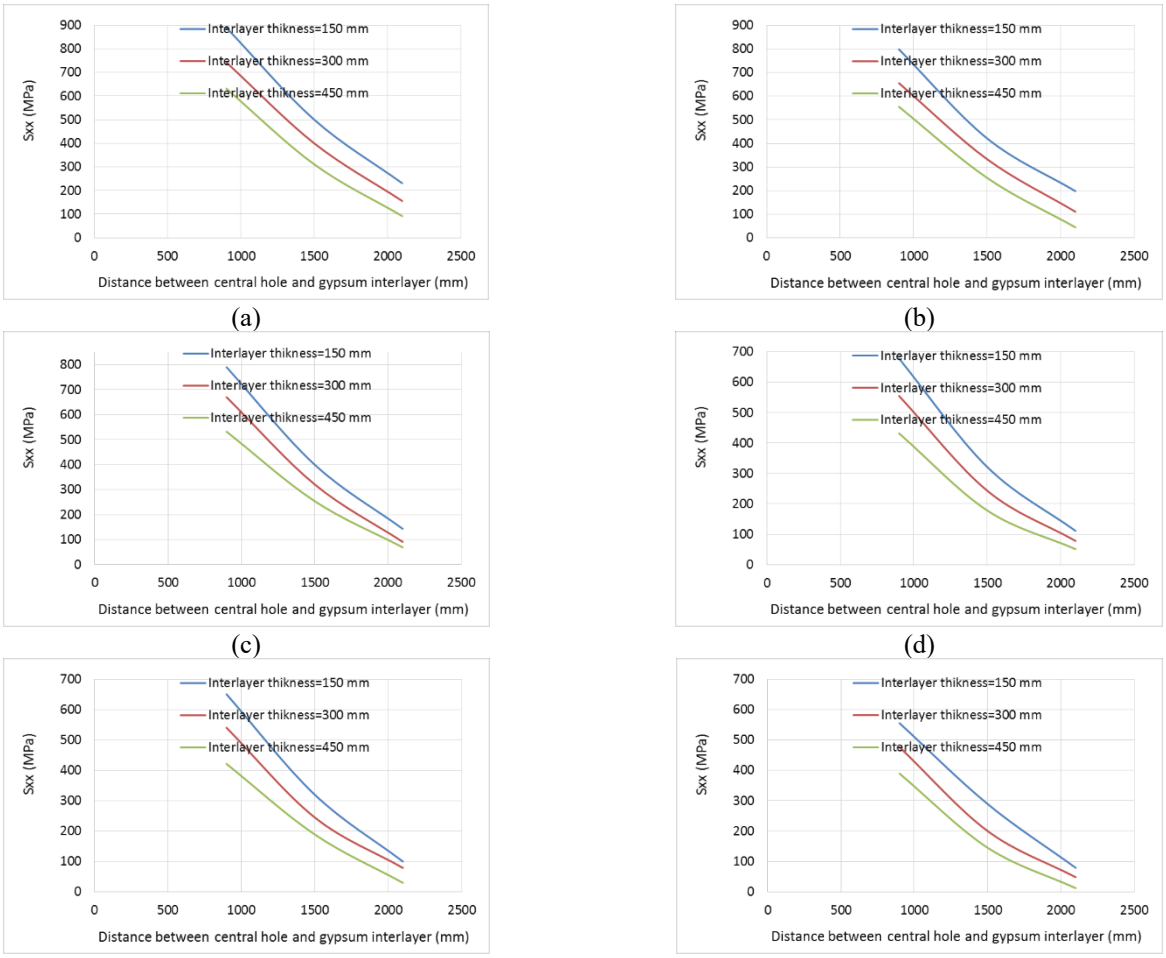

Fig. 15 Sxx varies for three distinct interlayer lengths of (a) 2000 mm, (b) 4000 mm, and (c) 6000 mm depending on the separation of the weak interlayer and the blast hole and the thickness of the hard interlayer

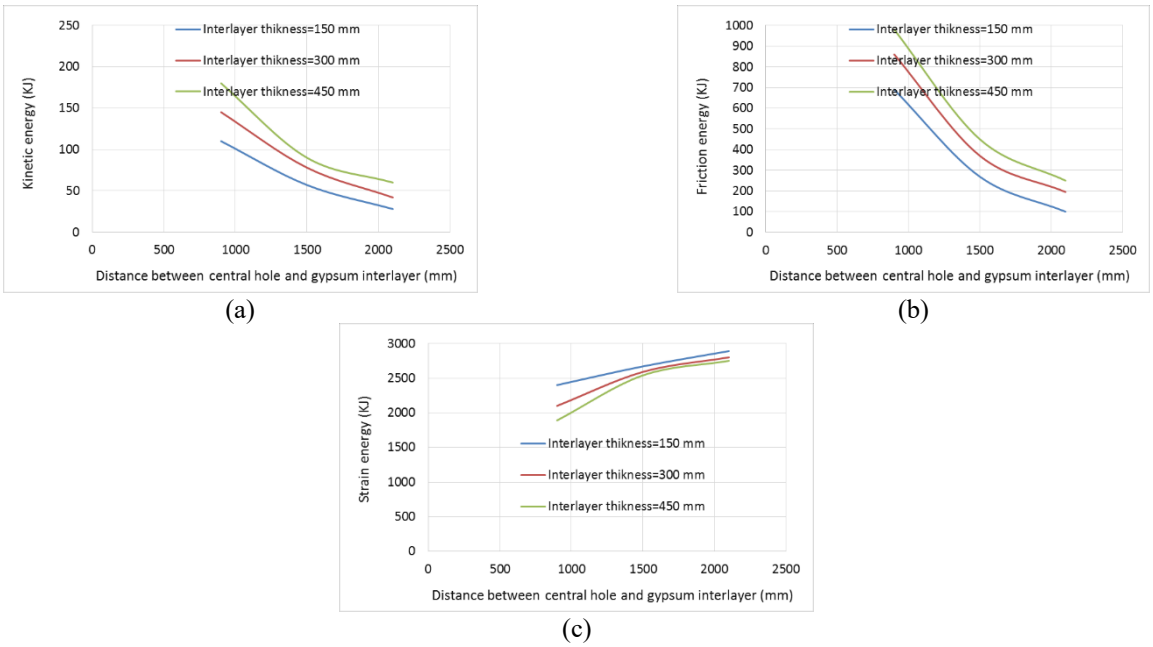

Fig. 16 (a) Kinetic energy fluctuation according to the separation between the center hole and the gypsum interlayer, (b) Adjustment in friction energy according to the separation between the center hole and the gypsum interlayer and (c) Modification of strain energy dependent on the distance between the central hole and the gypsum interlayer, where the length of the interlayer was 6000 mm

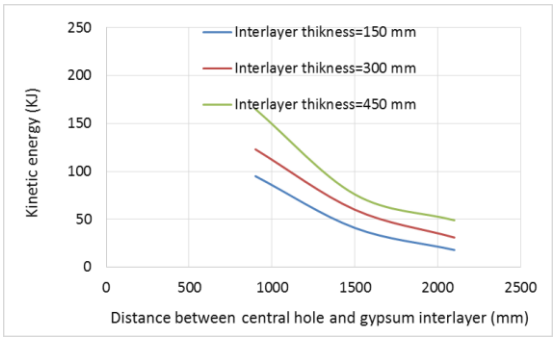

(a)

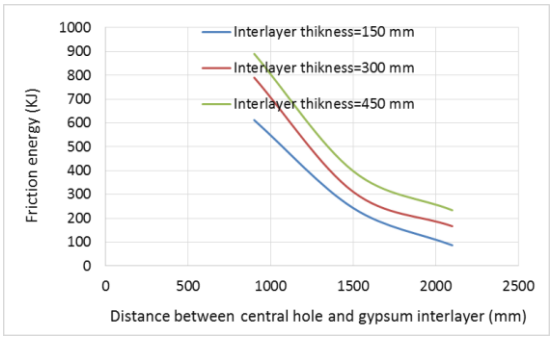

(b)

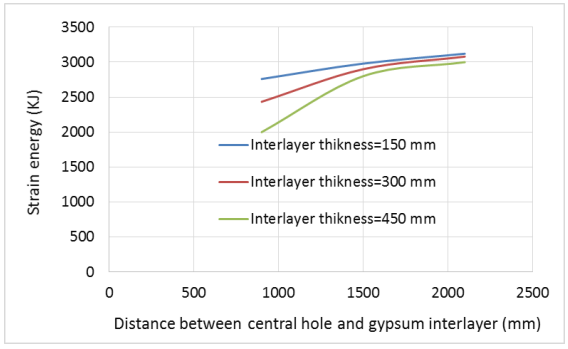

(c)

Fig. 17 (a) Kinetic energy fluctuation according to the separation between the center hole and the gypsum interlayer, (b) Adjustment in friction energy according to the separation between the center hole and the gypsum interlayer and (c) The variation in strain energy dependent on the distance between the center hole and the gypsum interlayer, where the length of the interlayer was 4000 mm

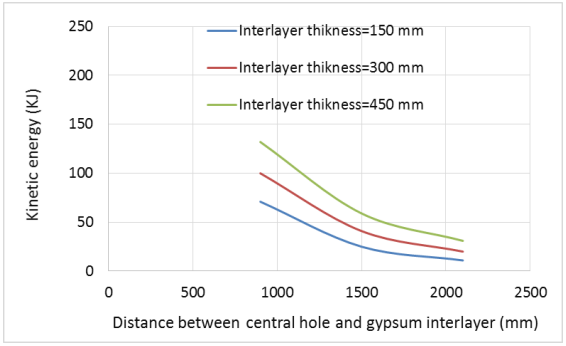

(a)

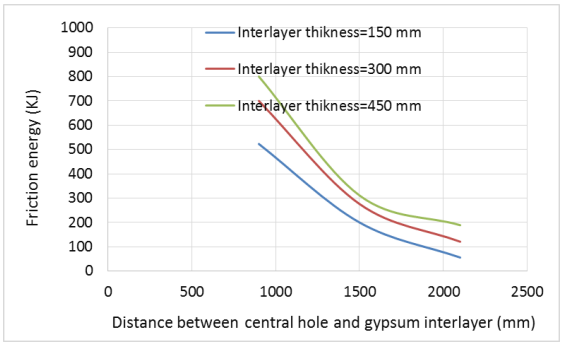

(b)

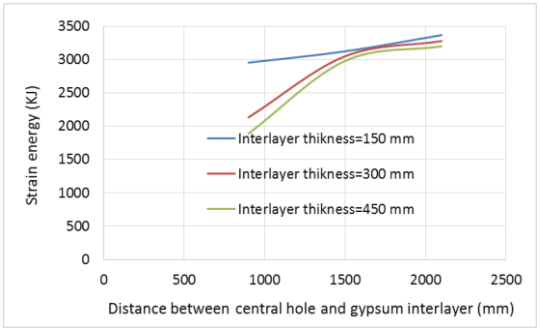

(c)

Fig. 18 (a) Kinetic energy fluctuation based on the separation of the gypsum interlayer from the center hole, (b) Modification in friction energy according to the separation between the center hole and the gypsum interlayer and (c) Alteration of strain energy depending on the separation of the gypsum interlayer from the center; the interlayer's length was 2000 mm

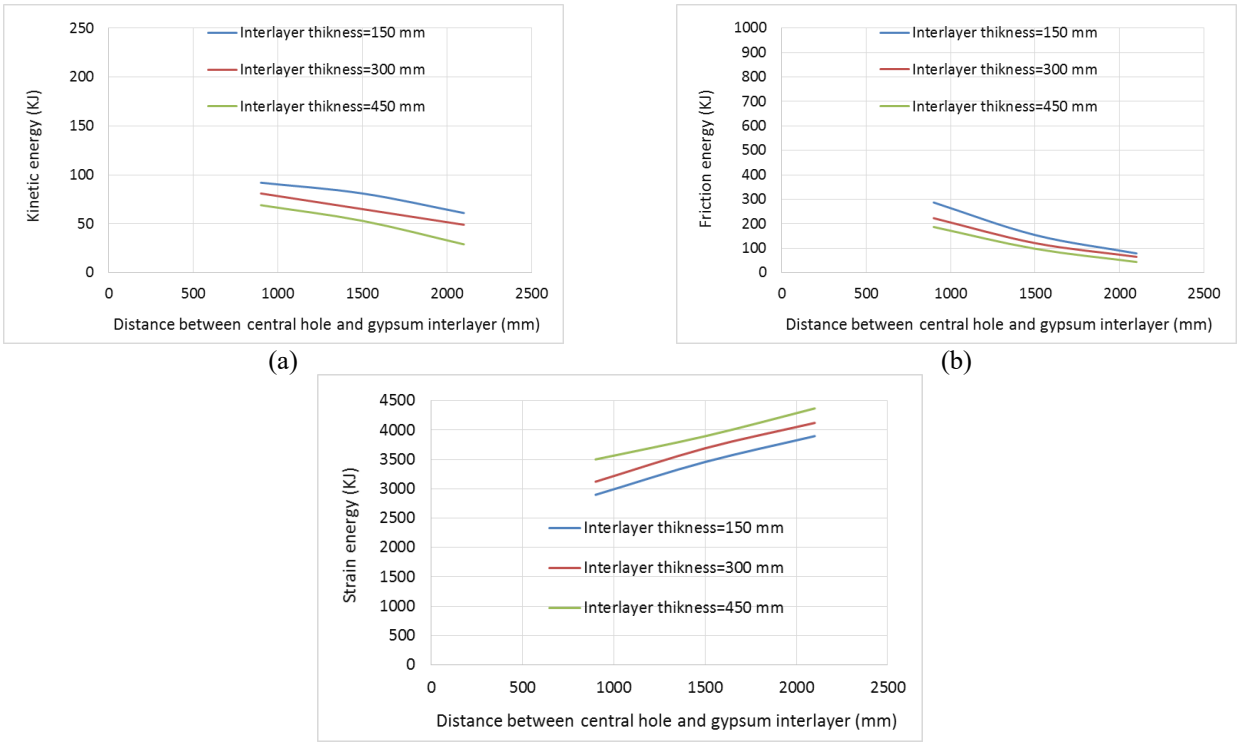

Fig. 19 (a) Kinetic energy fluctuation based on the separation of the gypsum interlayer from the center hole, (b) Variation in friction energy according to the separation between the center hole and the gypsum interlayer and (c) Modification of strain energy dependent on the distance between the central hole and the gypsum interlayer, where the length of the interlayer was 6000 mm

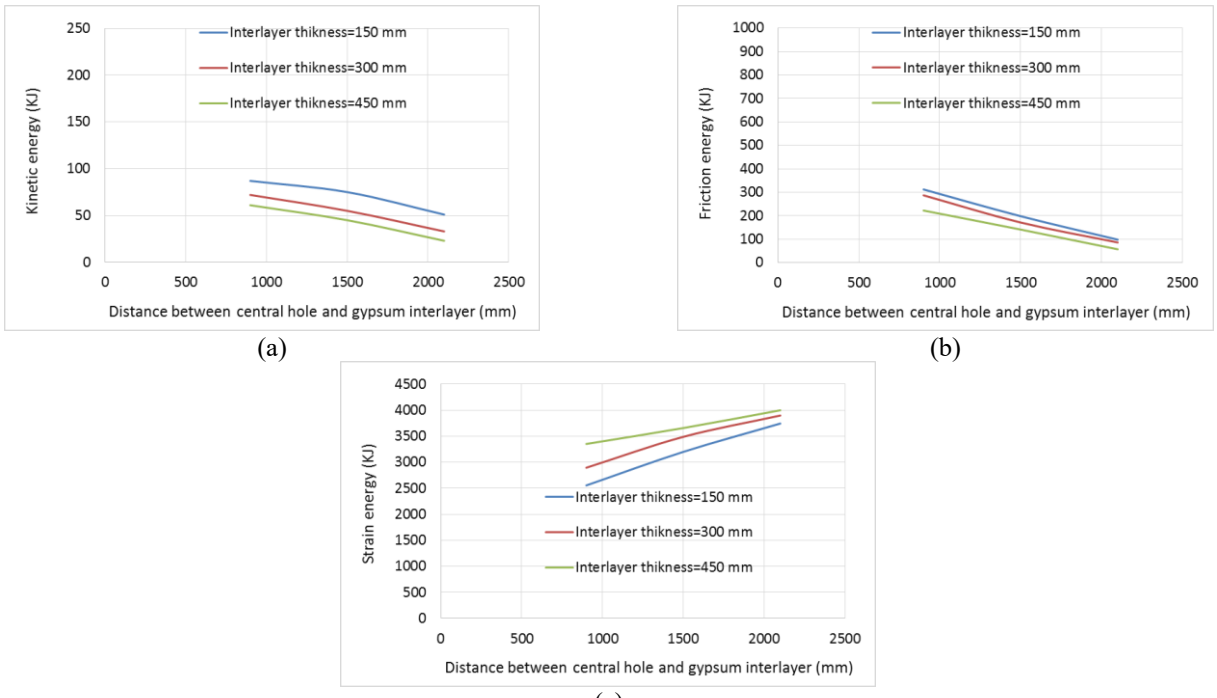

Fig. 20 (a) Kinetic energy fluctuation based on the separation of the gypsum interlayer from the center hole, (b) Variation in friction energy according to the separation between the center hole and the gypsum interlayer and (c) The variation in strain energy dependent on the distance between the center hole and the gypsum interlayer, where the length of the interlayer was 4000 mm

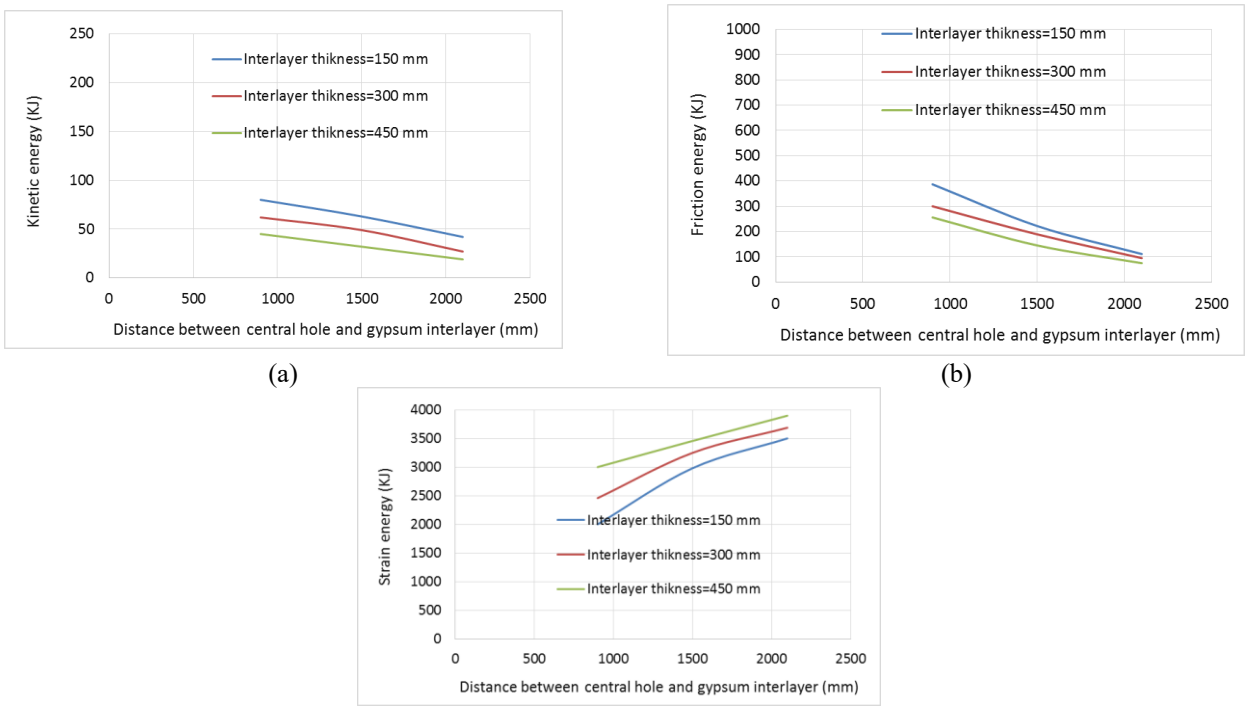

Fig. 21 (a) Kinetic energy fluctuation based on the separation of the gypsum interlayer from the center hole, (b) Adjustment of friction energy based somewhat on separation of the gypsum interlayer from the central hole and (c) Modulation of strain energy based also on separation of the gypsum interlayer from the center; the interlayer's length was 2000 mm

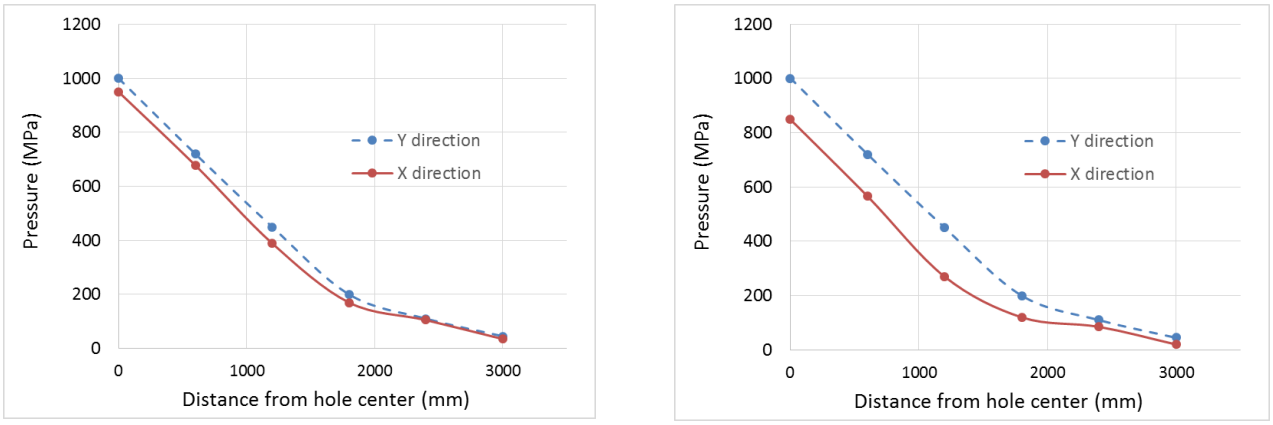

Fig. 22 Variation of the pressure at different distances from hole center in both of the X and Y axes for (a) hard concrete interlayer and (b) gypsum interlayer; interlayer length wad 6000 mm, and interlayer thickness was 450 mm and distance between interlayer and blasting hole was 900 mm

To assess how the characteristics of soft and hard rock layers influence rock blasting, Cui *et al.* (2022) performed numerical simulations of blasting experiments using PFC2D software, along with a particle expansion loading algorithm for support. They began by confirming the effectiveness of their blasting technique through a test involving a single-hole sandstone blast. Following this, they designed a model of composite strata consisting of both soft and hard rocks, and executed single-hole blasting trials on these layered formations, adjusting the thickness distribution of the soft and hard rock segments (Fig. 23).

The test results can be evaluated from three perspectives: the condition of the crack network, the internal stress within the rock mass, and the distribution of released energy. It can be observed that the proximity of the boundary between soft and hard rock near the blast hole has a significant effect on the effectiveness of the blast. When this issue is analyzed, the correlation between the number of cracks and their distance from the blast hole can be thoroughly examined.

When explosives are detonated in hard rock, the rock mass is subjected to relatively high pressure due to the

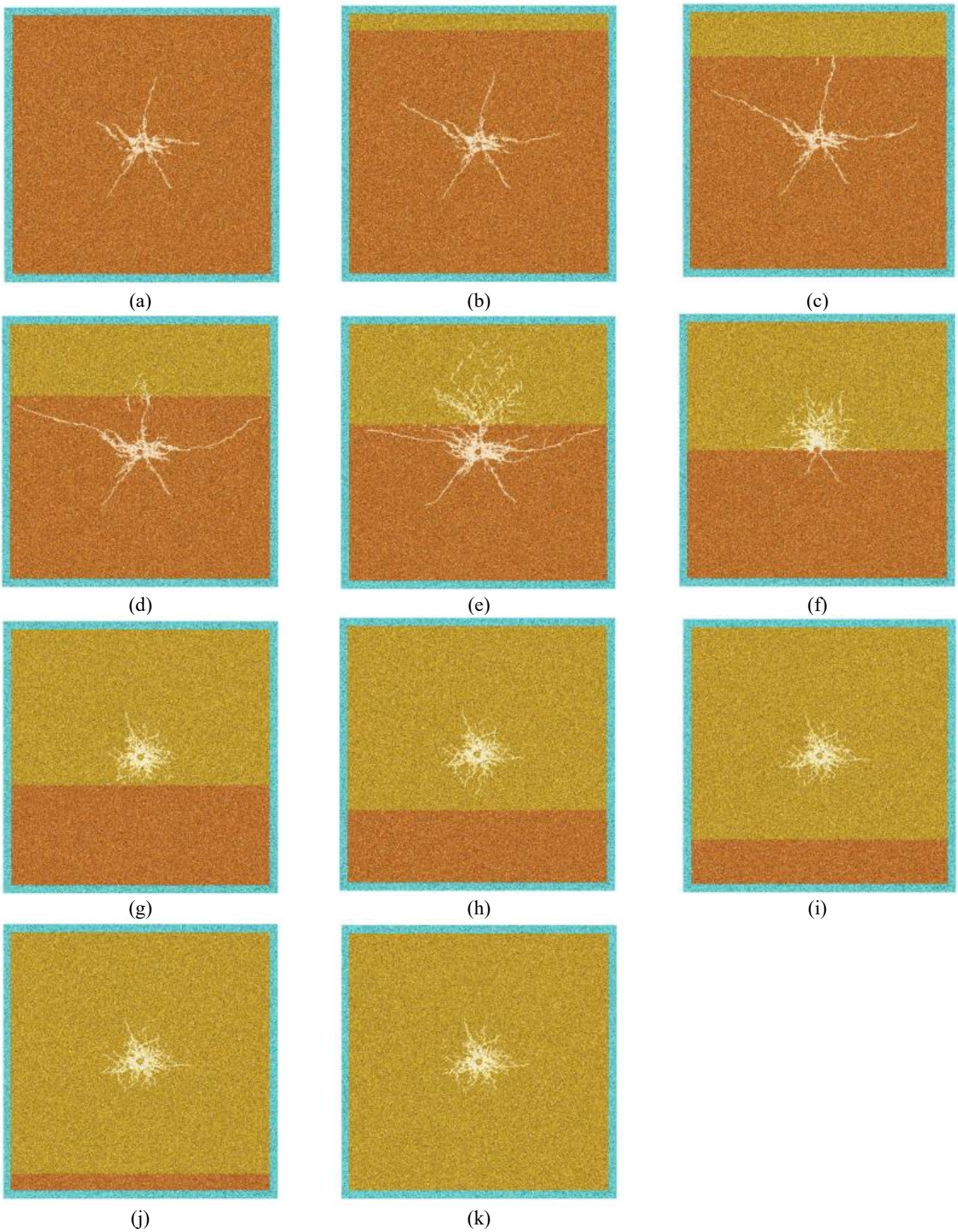

Fig. 23 blasting effects across various operational cases

presence of a structural plane approximately twice the radius of the blast hole crushing zone, resulting from stress wave reflection and superposition. In this case, when compared to a completely hard rock condition, it can be concluded that peak kinetic energy and peak friction energy increase by roughly 15 times and 2.6 times, respectively,

while peak strain energy decreases by 18%. Thus, these findings are found to be in good agreement with our findings, which include modeling and laboratory results. Additionally, the effect of hard and soft intermediate layers on wave attenuation has also been investigated.

4. Conclusions

This study examines the seismic behavior of joints filled with both hard and soft materials using numerical calculations and experimental testing. The key findings from the perspectives of blasting fracture effect as well as energy field are as follows:

(1) The concrete surrounding the bomb hole would be more completely destroyed whatever harder the interlayer was when it was placed in the simulation. When its position is fixed, the hard interlayer's ability to host concrete collapse and refract stress waves decreases as its thickness increases. In the same conditions, there should be an increase in fractures of around 1-2% when the distance between the hard interlayer and the blast hole is cut by 900 mm. The nearer the interlayer corresponds to the blast hole, the more damage the surrounding rock mass sustains when it is within a radius that is rough twice the size of the crushing region. The impact on the blasting result is minimal outside of this area. When the weak interlayer's location is fixed, as its thickness grows, so does its capacity to reflect stress waves and exacerbate concrete collapse. Whenever the separation of the weak interlayer and the blast hole is reduced by 900 mm, the number of fractures will rise by around 2-3% in the same conditions.

(2) According to the stress states of an object like the weak interlayer here on the left and right sides, the host concrete on both sides is under high stress whenever the weak interlayer is inside a radius of roughly two the crushing area multiplied, but this stress is low when such weak interlayer is outside of that radius. The host concrete from either side is under high stress whatsoever distances when the hard interlayer is included in the model.

(3) In the region where another interlayer is two times the radius of either the crushing surface or the blast hole, the thickness of something like the weak interlayer has a significant influence on the optimum kinetic energy, maximum frictional force, and maximum strain energy. The peak strain energy would rise by around 208 kJ due to an increase in interlayer thickness within this range, while the apex kinetic and friction energies would climb by about 21 and 12%, respectively. The three energies are often fairly steadily changing even when a hard interlayer is included in the model, and their position inside and thickness within the interlayer have less of an impact. When a hard interlayer is taken into account, the optimum kinetic energy and ultimate frictional energy will decrease by around 18 and 10% as the interlayer thickness increases, while energy at its highest strain will rise by about 290 kJ.

(4) By lengthening the interlayer in weak interlayers, the stress reduction was increased. By reducing the interlayer length, both the apex of kinetic energy and indeed the peak frictional energy were lowered. The interlayer length was shortened, which increased strain energy. By lengthening the interlayer in the hard interlayer, the stress attenuation decreases considerably. By lengthening the interlayer, the kinetic and friction energy peaks were both lowered. The interlayer length was lengthened, which increased strain energy. The soft interlayer model had a higher kinetic energy peak and overall friction energy peak than the hard interlayer model. Compared to the hard interlayer model, the soft interlayer model's strain energy peak was lower. This is because the host concrete's soft interlayer has a significant impact on dampening wave propagation.

(5) Results show that energy damping by a soft gypsum interlayer is greater than that by a hard concrete interlayer. Therefore, a soft interlayer could be used to dissipate wave energy on a large scale.

References

Abdellah, H. and Korichi, T. (2008), "Influence of joint direction and position of explosive charge on fragmentation", *Arabian J. Sci. Eng.*, 125-132.

Akbas, S. (2016), "Analytical solutions for static bending of edge cracked micro beams", *Struct. Eng. Mech*., **59**(3), 66-78. https://doi.org/10.12989/sem.2016.59.3.579.

Bai, T., Yang, H., Chen, X., Zhang, S. and Jin, Y. (2020), "In-situ monitoring and reliability analysis of an embankment slope with soil variability", *Geomech. Eng*., **23**(3), 261-273, https://doi.org/10.12989/gae.2020.23.3.261.

Barton, N. (1974), "A review of the shear strength of filled discontinuities in rock", *Norw. Geotech. Inst*., 105, 1-38.

Bidgoli, M.N. and Jing, L. (2014), "Anisotropy of strength and deformability of fractured rocks", *J. Rock Mech. Geotech. Eng*., **6**(2), 156-164. https://doi.org/10.1016/j.jrmge.2014.01.009.

Brekhovskikh, L.M. (1960), Waves in Layered Media. Academic, San Diego.

China Architecture & Building Press (2018), Numerical simulation technology and application with particle flow code (Pfc5.0), China Architecture & Building Press, Chong Shi, China.

Cui, J., Xie, L., Qin, Y., Liu, X., Qiao, W., Hu, Z., Wu, L., Qiu, L. and Huang, K. (2022), "Study on blasting characteristics of soft-hard rock strata basedon energy fields and particle expansion loading algorithm", *Geofluids*, **34**(3), 23-38. https://doi.org/10.1155/2022/5267143.

Fan, L. and Wong, L. (2013), "Stress wave transmission across a filled joint with different loading/unloading behavior", *Int. J. Rock Mech. Min. Sci*., **60**, 227-234. https://doi.org/10.1016/j.ijrmms.2012.12.046.

Flores-Johnson, EA., Wang, S., Maggi, F., El Zein, A., Gan, Y., Nguyen, G.D. and Shen, L. (2016), "Discrete element simulation of dynamic behaviour of partially saturated sand", *Int. J. Mech. Mater. Des*., **12**, 495-507. https://doi.org/10.1007/s10999-016-9350-5.

Ghazvinian, A., Sarfarazi, V., Schubert, W. and Blumel, M. (2012), "A study of the failure mechanism of planar non-persistent open joints using PFC2D", *Rock Mech. Rock Eng.*, **45**(5), 677-693. https://doi.org/10.1007/s00603-012-0233-2.

Golewski, G.L. (2024a), "Determination of fracture mechanic parameters of concretes based on cement matrix enhanced by fly ash and nano-silica", *Materials*, **17**(17), 4230. https://doi.org/10.3390/ma17174230.

Golewski, G.L. (2024b), "Using digital image correlation to evaluate fracture toughness and crack propagation in the mode I testing of concretes involving fly ash and synthetic nano-SiO2", *Mater. Res. Express*, **11**(9). https://doi.org/10.1088/2053-1591/ad755e.

Golewski, G.L. (2024c), "Comparison of fracture behavior of set concretes based on natural and crushed aggregates", *Mater. Res. Express*, **11**, 10. https://doi.org/10.1088/2053-1591/ad87b4.

Golewski, G.L. (2024d), "Effect of coarse aggregate type on the fracture toughness of ordinary concrete", *Infrastructures*, **9**(10), 185. https://doi.org/10.3390/infrastructures9100185.

Haeri, H. (2015a), "Influence of the inclined edge notches on the shear-fracture behavior in edge-notched beam specimens", *Comput. Concrete*, **16**(4), 605-623. https://doi.org/10.12989/cac.2015.16.4.605.

Haeri, H. (2015b), "Simulating the crack propagation mechanism of pre-cracked concrete specimens under shear loading conditions", *Strength of Mater.*, **47**(4), 618-632.

Haeri, H. (2015c), Erratum to: "Propagation mechanism of neighboring cracks in rock-like cylindrical specimens under uniaxial compression", *J. Min. Sci.*, **51**, 1062.

Haeri, H. (2015d), "Crack analysis of pre-cracked brittle specimens under biaxial compression", *J. Min. Sci.*, **51**(6), 1091-1100.

Ju, Y. (2007), "Study on stress wave propagation in fractured rocks with fractal joint surfaces", *Int. J. Solids Struct.*, **44**(13), 256-271. https://doi.org/10.1016/j.ijsolstr.2006.11.015.

Kouroussis, G., Verlinden, O. and Conti, C. (2011), "Finite-dynamic model for infinite media: Corrected solution of viscous boundary efficiency", *J. Eng. Mech.*, **137**, 509-511.

Li, J. and Ma, G. (2009), "Experimental study of stress wave propagation across a filled rock joint", *Int. J. Rock Mech. Min. Sci.*, **46**(3), 471-478. https://doi.org/10.1016/j.ijrmms.2008.11.006.

Li, X., Zou, Y. and Zhou, Z. (2014), "Numerical simulation of the rock SHPB test with a special shape striker based on the discrete element method", *Rock Mech. Rock Eng.*, **47**, 1693-1709. https://doi.org/10.1007/s00603-013-0484-6.

Li, Y., Zhou, H., Dong, Z., Zhu, W., Li, S. and Wang, S. (2018), "Numerical investigations on stability evaluation of a jointed rock slope during excavation using an optimized DDARF method", *Geomech. Eng.*, **14**(3), 271-281, https://doi.org/10.12989/gae.2018.14.3.271.

Liu, X. (2020), "Experimental and numerical study on pre-peak cyclic shear mechanism of artificial rock joints", *Struct. Eng. Mech.*, **74**(3), 221-234. https://doi.org/10.12989/sem.2020.74.3.407.

Ma, G., Li, J. and Zhao, J. (2011), "Three-phase medium model for filled rock joint and interaction with stress waves", *Int. J. Numer. Anal. Met.*, **35**(1), 97-110. https://doi.org/10.1002/nag.941.

Marketos, G. and O'Sullivan, C. (2013), "A micromechanics-based analytical method for wave propagation through a granular material", *Soil Dyn. Earthq. Eng.*, **45**, 25-34. https://doi.org/10.1016/j.soildyn.2012.10.003.

Naeimi, N., Bagher Tavakoli, M. and Sabbaghi-Nadooshan, R. (2021), "Design of non-volatile digital circuit with assuming magnetic tunneling junction and carbon nanotubes field-effect transistors devices", *Smart Struct. Syst.*, **27**(6), 983-990. https://doi.org/10.12989/sss.2021.27.6.983.

Öner, E., Şabano, B.Ş., Yaylacı, E.U., Adıyaman, G., Yaylacı, M. and Birinci, A. (2022), "On the plane receding contact between two functionally graded layers using computational, finite element and artificial neural network methods", *J. Appl. Math. Mech.*, **102**(2), e202100287, https://doi.org/10.1002/zamm.202100287.

Potyondy, D.O. and Cundall, P.A. (2003), "A bonded-particle model for rock",. *Int. J. Rock Mech. Min. Sci.*, **41**, 1329-1364.

Qian, J., Tong, Y., Mu, L., Lu, Q. and Zhao, H. (2020), "A displacement controlled method for evaluating ground settlement induced by excavation in clay", *Geomech. Eng.*, **20**(4), 275-285. https://doi.org/10.12989/gae.2020.20.4.275.

Resende, R., Lamas, L., Lemos, J. and Calçada, R. (2010), "Micromechanical modelling of stress waves in rock and rock fractures", *Rock Mech. Rock Eng.*, **43**, 741-761. https://doi.org/10.1007/s00603-010-0098-1.

Sarfarazi, V. and Haeri, H. (2017), "Direct and indirect methods for determination of mode I fracture toughness using PFC2D", *Comput. Concrete*, **20**(1), 39-47. https://doi.org/10.12989/cac.2017.20.1.039.

Sarfarazi, V., Abharian S. and Ghorbani, A. (2021), "A Physical test and PFC modelling of rock pillar failure containing two neighboring joints and one hole", *Smart Struct. Syst.*, **27**(1), 123-137. https://doi.org/10.12989/sss.2021.27.1.123.

Sekban, D.M., Yaylacı, E.U., Özdemir, M.E., Yaylacı, M. and Tounsi, A. (2025), "Investigating formability behavior of friction stir-welded high-strength shipbuilding steel using experimental, finite element, and artificial neural network methods", *J. Mater. Eng. Perform.*, **34**, 4942-4950. https://doi.org/10.1007/s11665-024-09501-8.

Shaowei, H., Aiqing, X., Xin, H. and Yangyang, Y. (2016), "Study on fracture characteristics of reinforced concrete wedge splitting tests", *Comput. Concrete*, **18**(3), 337-354. https://doi.org/10.12989/cac.2016.18.3.337.

Shu, X., Zhu, Z., Qu, S., He, L., Zeng, H., Zhang, C. and Tian, Y. (2025), "Anisotropic characteristics and deformation behaviors of layered rocks surrounding tunnel: A review", *J. Rock Mech. Geotech. Eng.*, In Press. https://doi.org/10.1016/j.jrmge.2025.03.009.

Shuraim, A.B., Aslam, F., Hussain, R. and Alhozaimy, A. (2016), "Analysis of punching shear in high strength RC panels–experiments, comparison with codes and FEM results", *Comput. Concrete*, **17**(6), 739-760. https://doi.org/10.12989/cac.2016.17.6.739.

Sinha, U. and Singh, B. (2000), "Testing of rock joints filled with gouge using a triaxial apparatus", *J. Rock Mech. Min. Sci.*, **37**(6), 963-981. https://doi.org/10.1016/S1365-1609(00)00030-7.

Thomas, C.N., Papargyri-Beskou, S. and Mylonakis, G. (2009), "Wave dispersion in dryb granular materials by the distinct element method", *Soil Dyn. Earthq. Eng.*, **29**(5), 888-897. https://doi.org/10.1016/j.soildyn.2008.10.002.

Toomey, A. and Bean, C.J. (2000), "Numerical simulation of seismic waves using a discrete particle scheme", *Geophys. J. Int.*, **141**(3), 595-604. https://doi.org/10.1046/j.1365-246x.2000.00094.x.

Wang, M. and Qian, Q. The attenuation law when the explosive stress wave transmit joint fissures. Selections from Academician Qian Qi-hu's theses, 335-340.

Wang, Y., Zhang, H., Lin, H., Zhao, Y., Li, X. and Liu, Y. (2020), "Mechanical behavior and failure analysis of fracture-filled gneissic granite", *Theor. Appl. Fract. Mec.*, **108**, 102674. https://doi.org/10.1016/j.tafmec.2020.102674.

Woo, J., Kim, D. and Na, W.B. (2015), "Application of numerical simulation of submersed rock-berm structure under anchor collision for structural health monitoring of submarine power

cables", *Smart Struct. Syst.*, **15**(2), 299-314, https://doi.org/10.12989/sss.2015.15.2.299.
Wright, P. (2010), "Assessment of London underground tube tunnels - investigation, monitoring and analysis", *Smart Struct. Syst.*, **6**(3), 239-262. https://doi.org/10.12989/sss.2010.6.3.239.
Wu, W., Li, J. and Zhao, J. (2012a), "Loading rate dependency of dynamic responses of rock joints at low loading rate", *Rock Mech. Rock Eng.*, **45**, 421-426. https://doi.org/10.1007/s00603-011-0212-z.
Wu, W., Li, J. and Zhao, J. (2013a), "Seismic response of adjacent filled parallel rock fractures with dissimilar properties", *J. Appl. Geophys.*, **96**, 33-37. https://doi.org/10.1016/j.jappgeo.2013.06.009.
Wu, W., Li, J. and Zhao, J. (2014), "Role of filling materials in a P-wave interaction with a rock fracture", *Eng. Geol.*, **172**, 77-84. https://doi.org/10.1016/j.enggeo.2014.01.007.
Wu, W., Zhu, J. and Zhao, J. (2012b), "A further study on seismic response of a set of parallel rock fractures filled with viscoelastic materials", *Geophys. J. Int.*, **192**(2), 671-675. https://doi.org/10.1093/gji/ggs055.
Wu, W., Zhu, J. and Zhao, J. (2013b), "Dynamic response of a rock fracture filled with viscoelastic materials", *Eng. Geol.*, **160**, 1-7. https://doi.org/10.1016/j.enggeo.2013.03.022.
Xue, Y., Li, X., Qiu, D., Ma, X., Kong, F., Qu, C. and Zhao, Y. (2019), "Stability evaluation for the excavation face of shield tunnel across the Yangtze River by multi-factor analysis", *Geomech. Eng.*, **19**(3), 283-293. https://doi.org/10.12989/gae.2019.19.3.283.
Yang, S.Q., Yin, P.F., Huang, Y.H. and Cheng, J.L. (2019), "Strength, deformability and X-ray micro-CT observations of transversely isotropic composite rock under different confining pressures", *Eng. Fract. Mech.*, **214**, 1-20. https://doi.org/10.1016/j.engfracmech.2019.04.030.
Yaylaci, E.U., Oner, E., Yaylaci, M., Ozdemir, M.E., Abushattal, A. and Birinci, A. (2022), "Application of artificial neural networks in the analysis of the continuous contact problem", *Struct. Eng. Mech.*, **84**(1), 35-48. https://doi.org/10.12989/sem.2022.84.1.035.
Yaylacı, M. (2016), "The investigation crack problem through numerical analysis", *Struct. Eng. Mech.*, **57**(6), 1143-1156,. https://doi.org/10.12989/sem.2016.57.6.1143.
Zamani, N. and El Shamy, U. (2011), "Analysis of wave propagation in dry granular soils using DEM simulations", *Acta Geotech.*, **6**, 167-182. https://doi.org/10.1007/s11440-011-0142-7.
Zhao, J. and Cai, J. (2001), "Transmission of elastic P-waves across single fractures with a nonlinear normal deformational behavior", *Rock Mech. Rock Eng.*, **34**, 3-22. https://doi.org/10.1007/s006030170023.
Zhao, J., Sun, L. and Zhu, J. (2012), "Modelling P-wave transmission across rock fractures by particle manifold method (PMM)", *Geomech. Geoeng.*, **7**, 175-181. https://doi.org/10.1080/17486025.2012.695402.
Zhao, X., Zhao, J., Hefny, A. and Cai, J. (2006), "Normal transmission of S-wave across parallel fractures with Coulomb slip behavior", *J. Eng. Mech. - ASCE*, **132**(6), 641-650. https://doi.org/10.1061/(ASCE)0733-9399(2006)132:6(641).
Zhou, H. and He, C. (2020), "Propagation law of stress wave and cracks in non-penetrating jointed rock mass: A numerical study based on particle flow code", *Geotech. Geol. Eng.*, **38**, 3967-3981. https://doi.org/10.1007/s10706-020-01271-z.
Zhu, J., Perino, A., Zhao, G., Barla, G., Li, J., Ma, G. and Zhao, J. (2011), "Seismic response of a single and a set of filled joints of viscoelastic deformational behaviour", *Geophys.*, **186**(3), 1315-1330. https://doi.org/10.1111/j.1365-246X.2011.05110.x.
Zhu, J., Zhao, X., Wu, W. and Zhao, J. (2012), "Wave propagation across rock joints filled with viscoelastic medium using modified recursive method", *J. Appl. Geophys.*, **86**, 82-87. https://doi.org/10.1016/j.jappgeo.2012.07.012.

CC